Chapter 5

Synthesis of magnetically recoverable polyaniline-based bifunctional solid-acid catalyst for the catalytic transformation of biomass-derived glucose into hydroxymethylfurfural

Abstract

A magnetically recoverable bifunctional catalyst (Fe_3O_4@SPAN) was successfully synthesized by incorporating Fe_3O_4 nanoparticles into polyaniline matrix while supporting sulfonic acid groups (-SO_3H) on the backbone of the polyaniline chain. The obtained materials were exhaustively characterized by FTIR, p-XRD, Raman spectroscopy, TGA, NH_3-TPD measurements, ICP-AES, VSM, XPS, SEM, EDX, HRTEM, and N_2 adsorption-desorption isothermal analysis and investigated for the conversion of *Saccharum spontaneum* derived glucose and banana peduncle derived glucose to HMF. Effects of reaction parameters were assessed using multivariate experimental designs viz., Response Surface Methodology (RSM) and Artificial Neural Network (ANN). The highest HMF yield of ~75% is obtained from glucose with complete inhibition of HMF rehydration to byproducts. Consecutive usage of the catalyst indicated that, after 5 cycles, the activity loss is not substantial in terms of HMF yield and glucose conversion. Furthermore, the reaction mechanism for the conversion of glucose to HMF was investigated using density functional calculations (DFT) and the results confirmed the role of Fe_3O_4 and -SO_3H on the transformation steps. This study emphasizes the potential significance of the simultaneous introduction of Lewis acidity and Brønsted acidity on a solid catalyst for the efficient conversion of renewable carbohydrates into fine chemicals.

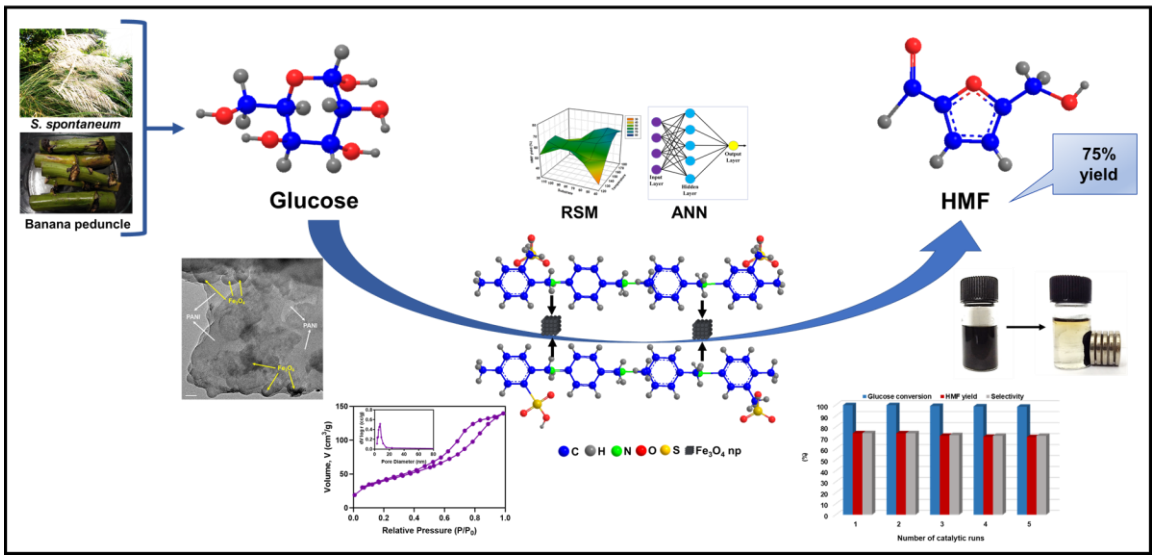

5.1. Introduction

In recent years, there has been great interest in the acid-catalyzed dehydration of biomass-derived carbohydrates to hydroxymethylfurfural (HMF), a potentially viable platform molecule that is a versatile intermediate for the synthesis of a wide variety of fine chemicals, liquid fuels, and monomers for high-value polymeric materials [1]. For instance, HMF can be converted into 2,5-Dimethylfuran (DMF) by selective hydrogenation reaction [2], 2,5-Furandicarboxylic acid (FDCA) by oxidation [3], levulinic acid (LA) by hydrolysis reaction [4], and C7-C15 liquid alkanes by aldol condensation followed by dehydration/hydrogenation reactions [5].

Simple carbohydrates such as glucose and fructose can be converted to HMF through different homogeneous and heterogeneous acid-base catalysts in monophasic or biphasic solvent systems. In comparison to glucose, fructose can be efficiently converted to HMF in a single step over Brønsted acid sites and a relatively higher yield has been achieved [6, 7]. However, because fructose is more expensive and has finite resources, glucose is favoured for the synthesis of HMF due to its low cost and availability [8]. The conversion of glucose to HMF occurs in two steps, viz., i) glucose isomerization to fructose through Lewis acidic sites of the catalyst, and ii) fructose dehydration to HMF through Brønsted acidic sites of the catalyst [9]. Although different homogeneous catalysts such as metal chlorides, inorganic acids, and ionic liquids have exhibited outstanding catalytic activity in the conversion of carbohydrates to HMF, their practical uses were restricted by disadvantages such as separation difficulties, waste treatment, reactor corrosion, and/or low recyclability [10, 11]. In this context, great attention has been paid to developing heterogeneous solid acid catalysts, typically inorganic solid acids for this conversion [12].

Metal oxides, particularly transition metal oxides (TiO_2, ZrO_2, NbO_2, etc.), have been commonly employed in the synthesis of HMF owing to their Lewis acidic characteristics, ease of preparation, low toxicity, and low cost [13, 14]. However, the productivity using metal oxide directly to catalyze glucose dehydration was relatively low due to the lack of appropriate Brønsted acidity. As a consequence, a variety of methods have been employed to modify metal oxides into mixed oxides, sulfated and phosphated oxides, nanoparticles, etc. in order to match the reaction requirement of efficient glucose conversion to HMF [12]. Nevertheless, under experimental conditions, the acid sites in inorganic solid acids or metal oxides are prone to be replaced by water molecules or leached, causing the catalysts to deactivate [15]. Polymeric materials, on the other hand,

have a wide range of uses as heterogeneous catalysts or supports. But due to inadequate surface acidity, functionalization of such materials with H_2SO_4, H_3PO_4, and HNO_3 to boost the Brønsted acid functional groups to facilitate fructose dehydration to HMF has been a frequent practise [6, 16]. However, typical sulfonated polymers, in which the sulfonic acid groups are chemically attached to the polymer chain, have exhibited great activity and stability for glucose dehydration [17]. In this respect, polyaniline (PANI), a fundamental polymeric material consisting of benzenoid amine and quinoid diimine structural units has found a range of catalytic uses such as nanoscale support for metal nanoparticles or complexes in Suzuki coupling or redox processes due to its ease of preparation and outstanding stability [18, 19].

Herein, we report an efficient bifunctional catalyst for the conversion of glucose to HMF: Fe_3O_4 incorporated sulfonated polyaniline (Fe_3O_4@PANI), with the coexistence of Lewis and Brønsted acid sites by integrating Fe_3O_4 nanoparticles into polyaniline matrix while supporting sulfonic acid groups (-SO_3H) on the backbone of the polyaniline chain. The catalytic performance of the catalyst was investigated in different catalytic systems. The structure, morphology, and physiochemical properties of the catalysts are characterized by means of FTIR, p-XRD, Raman spectroscopy, TGA, NH_3-TPD measurements, ICP-AES, VSM, XPS, SEM, EDX, HRTEM, and N_2 adsorption-desorption isothermal analysis. The reaction parameters affecting the yield of HMF such as reaction temperature, reaction time, catalyst loading, and substrate concentration were optimized using multivariate experimental designs viz., Response Surface Methodology (RSM) and Artificial Neural Network (ANN), as well as the reusability of the catalyst, was investigated. A probable reaction mechanism over the catalyst was also hypothesized based on the findings.

5.2. Experimental section

5.2.1. Materials

Ferric chloride ($FeCl_3.6H_2O$), ferrous chloride tetrahydrate ($FeCl_4.H_2O$), 1,6-hexane diamine ($H_2N(CH_2)_6NH_2$), aniline (AN), ammonium persulfate (APS), metanillic acid (MA) and hydrochloric acid (HCl) were purchased from Merck India Pvt. Ltd. All chemicals were used directly without further purification.

5.2.2. Synthesis of Fe_3O_4 nanoparticles

Fe_3O_4 nanoparticles were synthesized by the chemical co-precipitation method as depicted in Fig. 5.1. First, two solutions, one containing 0.033 mol dm^{-3} of $FeCl_3.6H_2O$ and 0.017 mol dm^{-3} of $FeCl_4.H_2O$ solution and the other containing 0.25 mol dm^{-3} of 1,6-hexane diamine (pH 12.1) aqueous solutions, were prepared separately. After that, the iron salt solution was mixed with the aqueous solution of 1,6-hexane diamine and a black precipitate was formed immediately. After vigorous stirring at constant temperature for 24 h, the precipitate was then filtered off with an Omnipore membrane filter from Millipore. The pH value of the filtrate was 11.3–11.5. To remove the excess amine molecules, the precipitate was washed with distilled water several times. The Fe_3O_4 nanoparticles were finally collected as a black powder after drying at room temperature.

5.2.3. Synthesis of Fe_3O_4@sulfonated polyaniline

Fe_3O_4@sulfonated polyaniline (Fe_3O_4@SPAN) catalyst was synthesized by using a surface-initiated polymerization method. An appropriate amount of Fe_3O_4 nanoparticles and MA were initially mixed with aniline/HCl solution (11 mmol aniline in 40 mL 1 M HCl) and then sonicated for 30 mins. Then a mixture of 10 mL 1.3 mmol APS solution and 10 mL 1M HCl solution was added dropwise into the above suspension. The polymerization reaction was carried out at 4°C for 22h. The resulting precipitates were washed with distilled water until the filtrate become neutral and then dried in a hot-air oven at 60°C to obtain x-Fe_3O_4@SPAN-y/z, where x represents the weight percentage of Fe_3O_4 loading and y/z represents the molar ratio of APS/(AN + MA) ranging from 6/3 to 12/3 to study the effect of sulfonic acid functionalization on 5-HMF yield [20]. Pure PANI and sulfonated PANI (SPAN) were also synthesized following the same procedure without the addition of Fe_3O_4 nanoparticles and MA and with the addition of MA, respectively. The synthesis procedure of the catalyst is depicted in Fig. 5.1.

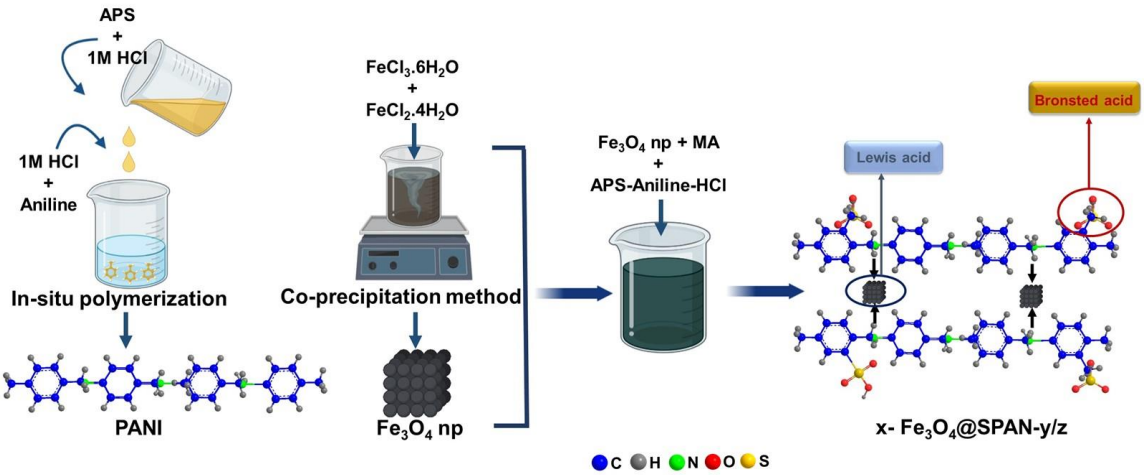

Fig. 5.1. *Schematic representation of x-Fe_3O_4@SPAN-y/z synthesis.*

5.2.4. Catalyst Characterization

Fourier transform infrared (FTIR) spectra were obtained in the Potassium Bromide (KBr) medium on a Perkin Elmer Spectrum 100 Optica FT-IR Spectrometer (USA). Typically, 5 mg of catalyst sample were ground with 95 mg pure KBr (5:95 w/w ratio) and pelletized with the help of a Qwik Handi-Press Kit. The KBr disc was then mounted in a quartz IR cell and read in the wavelength range of 500–4000 cm^{-1} with 32 scans at an effective resolution of 4 cm^{-1}, for each sample.

The X-ray diffractograms of the synthesized catalyst were obtained using an X-ray Diffractometer (Rigaku-Miniflex, Japan) with Ni filtered Cu Kα radiation (λ = 1.5406 Å) at the operating voltage and current of 40 kV and 15 mA respectively. Each sample was scanned over the 2θ range of 10°~50° and a scan rate of 1° min^{-1}. The p-XRD pattern of the catalyst was compared with the characteristic peaks of pure Fe_3O_4 np and the blank PANI.

The thermal stability of the catalysts was analyzed by thermogravimetric analysis (TGA) with respect to weight loss due to an increase in temperature. The analysis was performed by an STA 6000 Simultaneous Thermal Analyzer from Perkin Elmer (USA). For the analysis, the samples were gradually heated from room temperature to 700 ^oC at a heating rate of 20 ^oC min^{-1} in an ambient nitrogen environment.

The acidities of the prepared catalysts were investigated using NH_3-Temperature programmed desorption (NH_3-TPD) analysis. The analysis was performed on a Micromeritics, AUTOCHEM - 2950 instrument. At first, the catalyst was degassed for 1

hour at 150°C with a flow rate of 30 mL min^{-1} of He gas. The degassed sample was then saturated with NH_3 at a flow rate of 30 ml min^{-1} for 40 min at 50 ^oC. The sample was then heated for 1 hour at 100°C with a flow of He (30 mL min^{-1}) to remove any physisorbed NH_3 from the catalyst surface. Finally, the NH_3 desorption was monitored and the data was recorded on a thermal conductivity detector linked to a chemisorption device in the temperature range of 100 ^oC to 800 ^oC.

The surface area, pore size, and pore volume of the catalysts were calculated using Brunauer-Emmett-Teller (BET) method measured by N_2 physisorption with Quantachrome Instruments (NOVA 1000e). Furthermore, Raman spectroscopy measurements were carried out using a high-performance Renishaw inVia^{TM} Raman Spectrometer with a CCD detector, an optical microscope (Olympus MPlan N), and a 514 nm Modu-Laser Stellar-REN laser.

To measure the iron oxide content in the fresh and spent catalysts, the samples were digested in the presence of a strong acidic media, and the Fe (%) content was determined using Atomic Emission Spectroscopy (Agilent Technologies -Agilent 4200 MP -AES, USA) against a standard curve of Fe. Magnetic properties were determined by a vibrating sample magnetometer (VSM) (Lakeshore 7400 series).

The measurement of X-ray photoelectron spectroscopy (XPS) spectra was performed on an X-ray photoelectron spectrometer (Thermo Fisher Scientific Pvt. Ltd., ESCALAB Xi+, UK). Morphology study and elemental distribution of the catalyst were examined by a Scanning Electron Microscope (SEM) (JSM-6390, JEOL, Singapore) and SEM-EDX (SEM-Energy Dispersive X-ray Diffraction spectroscopy), respectively. Pseudo-colors were used to generate the Elemental map to illustrate the elemental distribution in the synthesized catalyst. The morphology of the synthesized catalyst was further analysed using transmission electron microscopy (FEI Company, USA). For this, the sample was ground in an agate mortar, and a small amount was dispersed in anhydrous ethanol, which was dispersed using ultrasound. The suspension was then absorbed by a capillary tube into the copper network with carbon film suspended. After drying, it was observed in the electron microscope chamber. Their average dimensions were determined from the TEM images using the Image J (NIH) processing suite.

5.2.5. Reaction procedure using Multivariate Experimental Design

All the catalytic glucose conversion reactions were performed in a 50 ml round bottom flask located in a temperature-controlled oil bath and equipped with a magnetic stirring bar. In a typical experiment, an appropriate amount of glucose and catalysts were loaded into the flask along with a 5 mL solvent, and the reaction mixture was vigorously stirred at 300 rpm at a specific reaction temperature for a given reaction time (according to the experimental design). After completion of the reaction, the mixture was immediately put into ice water and cooled to room temperature. The catalyst was then separated by the application of an external magnetic field, filtering the solution through a 0.2 m syringe filter.

Response surface methodology:

RSM statistical approach was used to investigate the effect of independent experimental factors on glucose dehydration reaction while also achieving the optimum reaction condition [21, 22]. For this, the effects of univariate and multivariate interactions among the experimental factors (temperature, reaction time, catalyst loading, and substrate concentration) on HMF yield were studied through RSM based on Central Composite Design (CCD). A total of 21 experiments were considered for the quadratic model with four components and five levels. The statistical software package, Design-Expert 7.0 (Stat-Ease Inc., USA) was used to do the analysis of variance (ANOVA), regression analysis, design of experiment, and graphical analysis. The dehydration reaction data was modelled using the second-degree polynomial equation given below to reflect the relationship between the predicted response and experimental components [23].

$$Y = b_0 + \sum_{i=1}^{n} b_i X_i + \sum_{i=1}^{n} b_{ii} X_i^2 + \sum_{i=1}^{n} \sum_{i>j}^{n} b_{ij} X_i X_j$$

where n is the total number of variables, X_i and X_j are the coded values, b_0 is the model constant, Y is the predictive response, b_{ii} is the interaction coefficients, b_i is the linear coefficient, and b_{ij} is the quadratic coefficient.

Artificial Neural Networks modelling:

The RSM dataset was then combined with a three-layer feed-forward Multi-Layered-Perceptron (MLP) utilizing an artificial neural network (ANN) *via* MATLAB R2013a

computer suite (MathWorks USA) to predict the influence of multivariate associations under various reaction conditions on HMF yield. The network consists of three layers: an input, a hidden, and an output layer. A Levenberg Marquardt (LM) back-propagation learning system with tan sigmoid function (tansig) in the hidden layer and linear transfer function (purelin) in the output layer along with the neuron numbers in the input and output layers determined by the relative importance of the parameters detected in RSM dataset was used to create the neural system.

Model performance indices

To choose the best predictive model for the investigational data, the performance metrics of RSM and ANN modelling predictions were employed. Table 5.8 shows the results of the analysis, which employed seven statistical error functions that performed well. The assessment indices used were evaluated based on the information set used [24]. Furthermore, a relative parity map was employed to show specific deviation sites between RSM and ANN model estimates based on the investigative data.

5.2.6. Substrate and product analysis

The substrate and the reaction product were analysed using high-performance liquid chromatography (HPLC, Thermoscientific) equipped with an Accucore Hilic Amide column (150 X 4.6 mm) and an RI detector. A volume of 20 µl of the samples was injected into the column at a temperature of 65°C through the mobile phase of 0.5 mM H_2SO_4 at a flow rate of 0.6 mL per minute. Calibration curves obtained from standard glucose solutions and standard HMF solutions run under similar experimental conditions were used to calculate the glucose and HMF concentration.

The carbohydrates conversion, the HMF selectivity, and yield were evaluated by using the following equation.

$$\text{Conversion of glucose (\%)} = \frac{[Carbohydrates] \times V - [Carbohydrates]' \times V}{[Carbohydrates] \times V} \times 100$$

$$\text{Yield of HMF (\%)} = \frac{[C] \times V}{[Carbohydrates] \times V} \times \frac{M_a}{M_b} \times 100$$

$$\text{HMF Selectivity (\%)} = \frac{Yield}{Conversion} \times 100$$

where [Carbohydrates] was the initial concentration of carbohydrates in solution; [Carbohydrates]' was the final concentration of carbohydrates in solution; [C] was the final concentration of HMF. V was the volume of the mixture solution; M_a was the molecular weight of glucose; M_b was the molecular weight of HMF.

5.2.7. Catalyst reusability test

The stability of the Fe_3O_4@SPAN catalyst was tested by reusing the recovered catalyst in a series of experiments. After each run, the catalyst was separated by the application of an external magnetic field, thoroughly washed with water and ethanol, and then dried in a hot-air oven at 60°C. The reaction for each cycle was carried out under the optimal conditions obtained using a multivariable experimental design.

5.2.8. Computational details

The structures were geometry optimized employing density functional theory (DFT) method using the Becke, 3-parameter, Lee–Yang–Parr (B3LYP) functional [25, 26] along with LANL2DZ basis set [27]. To obtain zero-point energies, thermochemical parameters and different mode of vibrational frequencies, further frequency calculations were performed on all the optimized species at the same level of theory. All the quantum calculation were executed using the Gaussian 09 software [27].

5.3. Results and discussion

5.3.1. Comparison of catalytic activity of different synthesized catalysts and in different solvents based on HMF yield

At first, different synthesized catalysts were evaluated based on glucose conversion and HMF yield under a specific reaction condition (Fig. 5.2). As shown in Fig. 5.2 a, the catalytic activity of PANI for the conversion of glucose to HMF was very poor, with only 20.1% glucose conversion and 1.6% HMF yield was achieved. The SPAN catalyst formed by sulfonation of PANI did not add much to process efficiency, yielding just 1.7% HMF. The poor yield in the case of PANI might be attributed to the absence of any Lewis/Brønsted acidic sites, which are required to drive the reaction, whereas SPAN yielded low product due to insufficient conversion of glucose to fructose owing to the lack of Lewis acidic sites. However, the conversion reaction in both cases was most likely related to the reaction temperature and reaction time only. Fe_3O_4 nanoparticles as catalysts produced a significant increase in HMF yield to 29.4%. As discussed in Chapter 2, the

route from glucose to HMF passes through isomerization followed by dehydration. It can be confirmed from the NH_3-TPD results (Fig. 5.6 a) that Fe_3O_4 nanoparticles possessed weak, moderate, and strong acidic sites and therefore performed the conversion reaction well. The Fe_3O_4 nanoparticles alone showed 80.6% glucose conversion, while only 29.4% HMF yield was achieved. The reason for lower HMF yield could be considered due to the lack of adequate Brønsted acid sites in this catalyst [28]. Upon functionalization of sulfonic acid groups on Fe_3O_4 doped PANI the resulting functionalized Fe_3O_4@PANI catalyst produced a significant increase in the yield of HMF (72.7%) which specified the catalytic effect of Brønsted acid sites generated due to the functionalization of -SO_3H groups on PANI. This could be observed in the NH_3-TPD graph of 15-Fe_3O_4 @SPAN-9/3 catalyst (Fig. 5.6 a) with high-intensity peaks as compared to Fe_3O_4 np catalysts due to the formation of acidic groups such as -SO_3H groups on PANI. The formation of -SO_3H groups has been discussed in the section below.

The effect of Fe_3O_4 wt% loading on the catalytic activity of x-Fe_3O_4@SPAN-y/z catalyst is shown in Fig. 5.2 b. It is clear from Fig. 5.2 b that with an increase in Fe_3O_4 wt% from 5% to 15%, the glucose conversion increased progressively, reaching 98.70% and subsequent HMF yield of 72.70%. Beyond that, a slight reduction in glucose conversion (8.58%) was observed. With a further increase in Fe_3O_4 wt% loading, glucose conversion decreased further, reaching 86.30% at 30 wt% of Fe_3O_4 loading. Likewise, the HMF yield followed a decreasing trend with an increase in Fe_3O_4 loading. This might be explained by the fact that when more Fe_3O_4 is accessible, the concentration of the Lewis acidic sites in the catalyst increases, and HMF undergoes greater rehydration on the PANI surface, producing more byproducts (levulinic acid and formic acid) in the reaction route.

The effect of the quantity of sulfonic acid group functionalization on 15-Fe_3O_4@SPAN-y/z catalyst by varying the molar ratio of APS/(AN+MA) is shown in Fig. 5.2 c, wherein y/z represents the molar ratio of APS/(AN + MA) ranging from 6/3 to 12/3. A relatively low glucose conversion and HMF yield were observed when the ratio was 6/3. With an increase in the ratio from 6/3 to 9/3, the glucose conversion and HMF yield reached 98.70% and 72.70%, respectively. However, further increasing the molar ratio to 12/3 did not result in an increase in the HMF yield, in fact, a minor drop was detected, which might be attributed to the additional conversion of HMF to other by-products at high acid density. Indeed, for the conversion reaction using 15-Fe_3O_4@SPAN-9/3 catalyst, the reaction solution exhibited insignificant leaching of Fe species (2.03 ppm), confirming

their high catalytic stability. Taking all of these aspects into account, it was determined that the 15-Fe_3O_4@SPAN-9/3 catalyst was better suited for HMF production and was employed to further investigate the reaction parameters.

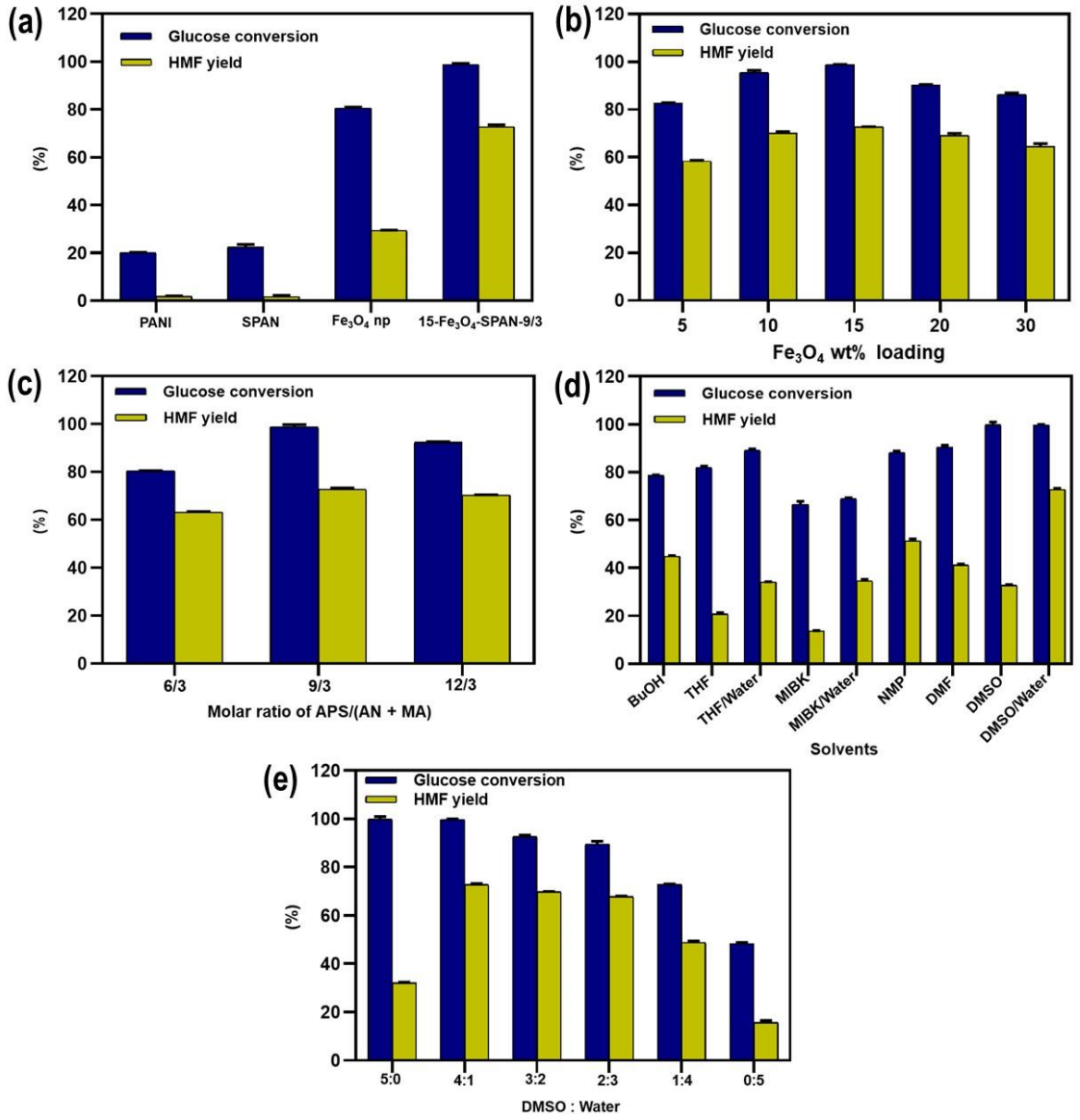

Fig. 5.2. *Comparative analysis of the catalytic activity of different catalysts (a), the effect of Fe_3O_4 wt% loading on the glucose conversion and HMF yield (b), the effect of sulfate functionalization on 15-Fe_3O_4@SPAN-y/z catalyst (c), the effect of different single-phase and biphasic solvents on the glucose conversion and HMF yield (d), influence of the inorganic phase to organic phase (MIBK) ratio on the glucose conversion and HMF yield (e) (reaction conditions: 80 mM glucose, 40 mg 15-Fe_3O_4@SPAN-9/3, 150°C, 4h).*

To examine the effect of solvents in the glucose conversion processes, a number of single-phase and two-phase solvents with varying ratios were used in the reaction. As

seen from Fig. 5.2 d, there was a noticeable difference in HMF yields in different solvents, elucidating a significant solvent impact. After the reaction at 150°C for 4 h, the yield of 5-HMF in the monophasic solvents was considerably lower than that in the biphasic solvents. With MIBK and THF as solvents, 15-Fe_3O_4@SPAN-9/3 had poor catalytic activity, which might be due to the decreased solubility of the substrate. However, with the addition of water as a co-solvent with MIBK and THF, the HMF yield% is observed to be almost doubled. Glucose conversions were quite high in BuOH, NMP, and DMF due to the high solubility of reactants, however, the poor 5-HMF yield was due to the presence of side reactions and the creation of humins [29]. The glucose conversion in DMSO reached > 95%, suggesting high solubility of reactant, however, the HMF yield is very low (32.7%) compared to the biphasic system (DMSO/Water). The poor HMF yield was caused due to the occurrence of side reactions and the synthesis of humins. In the biphasic solvent containing DMSO and water 72.7% HMF yield was obtained with a selectivity of 72.87%. In a biphasic reaction system, HMF was generated progressively in the inorganic phase with continuous extraction into the organic phase to accomplish substrate and product separation and as a consequence, it significantly facilitated the HMF yield [30].

The impact of the inorganic phase to organic phase ratio on the HMF yield is shown in Fig. 5.2 e. The low HMF yields in single-phase DMSO or water solvents suggest that condensation processes occur when reactants and products are present in the same phase. Organic solvents may hold more HMF molecules than inorganic solvents, as evidenced by the fact that the HMF yield in DMSO was higher than that in water solution. In conclusion, comparative studies were used to identify the ideal volume ratio of DMSO and water solution (4:1).

5.3.2. Catalysts characterization

The FTIR spectra of the synthesized Fe_3O_4 np, PANI, SPAN, and 15-Fe_3O_4@SPAN-9/3 are shown in Fig. 5.3 a. The characteristic absorption bands at 3437 cm^{-1} and 1632 cm^{-1} observed in all the spectra correspond to the O-H stretching and bending vibrations of the adsorbed water on the materials. The band at 584 cm^{-1} in the FTIR spectra of Fe_3O_4 np due to Fe-O stretching vibration is also present in the spectra of 15-Fe_3O_4@SPAN-9/3 nanocomposite [31]. From Fig. 5.3 b it is seen that for PANI, SPAN, and 15-Fe_3O_4@SPAN-9/3 the bands at 1575 and 1504 cm^{-1} are associated with the stretching mode of C=C in the benzenoid and quinoid rings, respectively [32]. The band at 1307 cm^{-}

[1] corresponds to the C-N stretching of secondary aromatic amine, while the band at 1154 cm^{-1} is ascribed to the –N= quinoid =N– stretching mode [33]. The characteristic bands at 1036, 693, and 619 cm^{-1}, in SPAN and 15-Fe_3O_4@SPAN-9/3 are assigned to the S=O, S–O, and C–S stretching vibrations, respectively, and are indicative of the presence of –SO_3H groups in the nanocomposite [20].

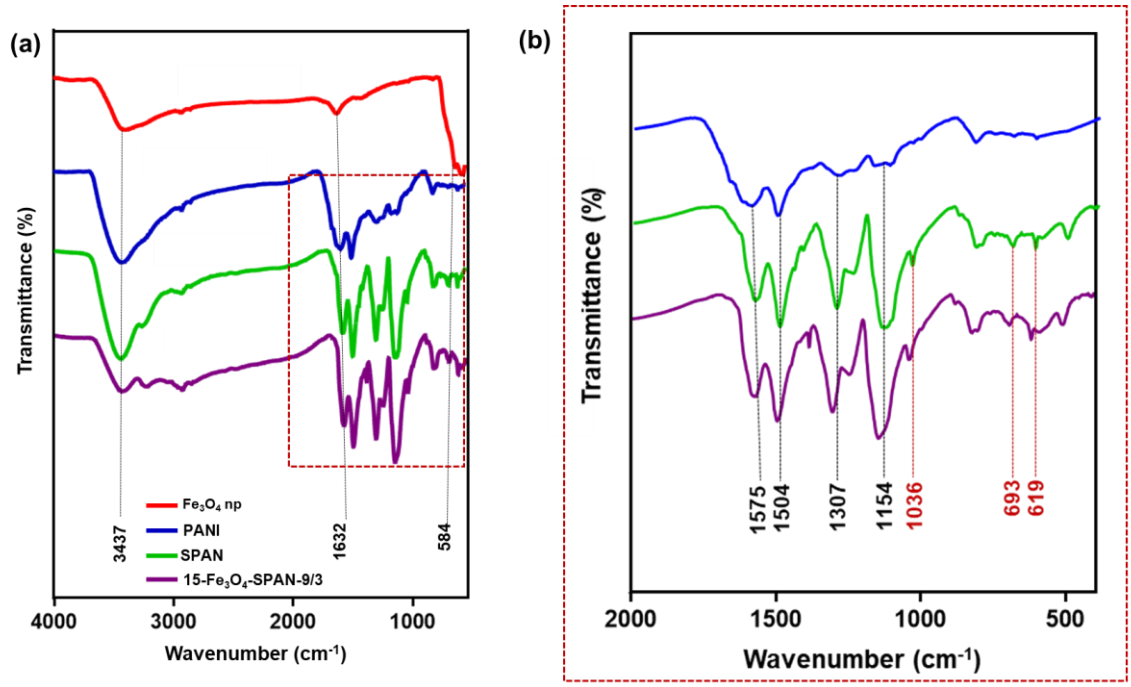

Fig. 5.3. *FTIR spectra of the synthesized catalysts (a) and magnified view of the absorption band area of PANI, SPAN, and 15-Fe_3O_4@SPAN-9/3 from 2000-400 cm^{-1} (b).*

The p-XRD patterns of the synthesized Fe_3O_4 np, PANI, SPAN, and 15-Fe_3O_4@SPAN-9/3 are shown in Fig. 5.4 a. The diffraction peaks of Fe_3O_4 nanoparticles and 15-Fe_3O_4@SPAN-9/3 at 2θ= 30.13°, 35.48º, 43.12°, 53.9°, and 62.81º can be assigned to the (220), (311), (400), (511) and (440) planes, respectively of a cubic spinel unit cell that match well with the standard Fe_3O_4 pattern [34]. The peak broadening of the p-XRD pattern suggests that the resultant crystallites are extremely small in size. The average crystallite size of Fe_3O_4 nanoparticles was calculated using Scherrer's formula to be 22.6 nm, which is in good agreement with the value of 23.7 nm of the mean particle sizes found by TEM images. No other peaks of any additional phases are observed indicating that the product is quite pure. The p-XRD patterns of PANI, SPAN, and 15-Fe_3O_4@SPAN-9/3 show a typical amorphous structure with a diffraction peak at 2θ of 25.7° and a smaller crystallographic spacing in SPAN (0.160 nm) and 15-Fe_3O_4 @SPAN-9/3 (0.160 nm)

compared to PANI (0.172 nm) suggests the obvious presence of $–SO_3H$ groups [20]. In addition, the d-value of lattice spacing of (311) was measured to be ~0.233 nm for both Fe_3O_4 nanoparticle and 15-Fe_3O_4@SPAN-9/3 nanocomposite by employing the Bragg equation which is in agreement with the corresponding standard value of 0.253 nm [35].

Raman spectroscopy revealed the molecular structure of the surface of magnetic nanocomposite materials Fig. 5.4 b. The Raman spectra of Fe_3O_4 nanoparticle and 15-Fe_3O_4@SPAN-9/3 nanocomposite, show four peaks at 698, 574, 512, and 410 cm^{-1} which are attributed to magnetic core [36]. The broad band at 800 cm^{-1} in the spectra of PANI, SPAN, and 15-Fe_3O_4@SPAN-9/3 refers to benzene ring deformation. Furthermore, a strong band appeared around 1587 cm^{-1} which is ascribed to the C=C stretching vibration in the quinonoid ring [37].

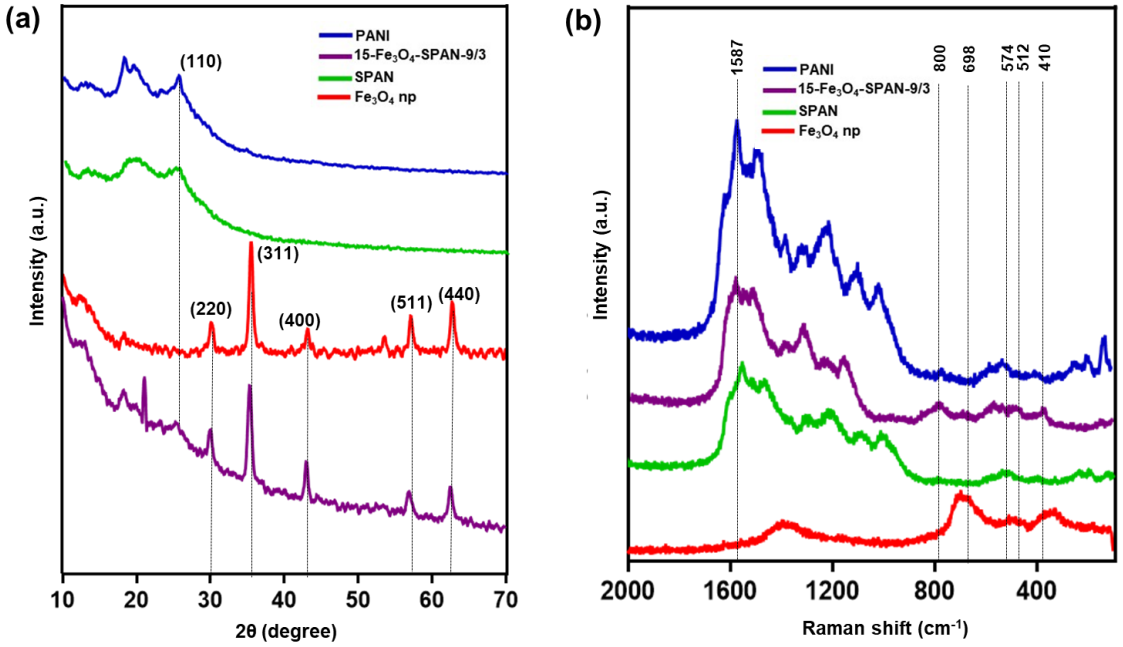

Fig. 5.4. *p-XRD patterns (a) and Raman spectra (b) of the synthesized catalysts.*

Fig. 5.5. shows the TGA results of PANI, Fe_3O_4, and 15-Fe_3O_4@SPAN-9/3. For PANI (Fig. 5.5 a), there are three major stages for weight loss at around 100°C, 250°C, and 500°C, which are assigned to the release of moisture, dopant (HCl), and the degradation of the polymer molecule, respectively. Fig. 5.5 b reveals that the Fe_3O_4 nanoparticle is very stable as no major decomposition takes place from 100-580°C. The weight loss after 580°C is most likely due to the phase change from Fe_3O_4 to FeO. At temperatures above 580°C, the phase diagram of the Fe-O system indicates that FeO is the

most stable species [38]. On the other hand, the decrease in weight from room temperature to 100°C was caused by the elimination of adsorbed water and any traces of organic solvents present in the sample [39]. In the TGA curve of 15-Fe_3O_4@SPAN-9/3 catalyst, there are two major stages of weight loss at around 100°C and 500°C, which are attributed to the removal of absorbed moisture content and the degradation of PANI, respectively. In general, the TGA analysis suggests that the synthesized catalyst is quite stable at high reaction temperatures.

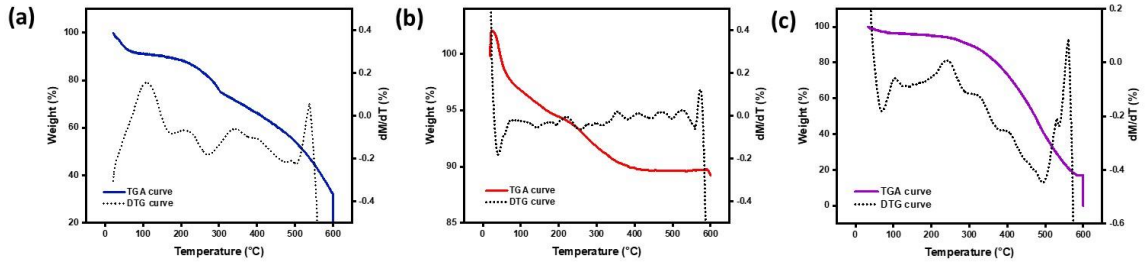

Fig. 5.5. *TGA and DTG curves of PANI (a), Fe_3O_4 np (b), and 15-Fe_3O_4@SPAN-9/3 catalyst (c).*

The surface acidities of PANI, Fe_3O_4, and 15-Fe_3O_4@SPAN-9/3 were analysed by NH_3-TPD, and respective results are given in Fig. 5.6 a and Table 5.1. The comparative position of the peak in the NH_3-TPD profile indicates the amount of energy required for NH_3 desorption which is directly proportional to the acidic strength of the catalyst [40]. In PANI, no such distinct peak was observed except for a broad hump. NH_3-TPD profile of Fe_3O_4 shows a small intensity peak around 311°C that might be attributed to the existence of weak acidic sites in the catalyst. In addition, peaks at 453°C and 674°C could be due to the NH_3 desorption from moderate and strong acidic sites, respectively. The NH_3-TPD profile of 15-Fe_3O_4@SPAN-9/3 is quite similar to that of Fe_3O_4 but with high-intensity peaks that signify a relatively high concentration of acidic sites. In fact, the strong NH_3 desorption peak with distinctly high intensity at higher temperatures (~ 674°C) signifies the presence of a large number of strong acid sites on the 15-Fe_3O_4@SPAN-9/3 catalyst, owing to the sulfonation modification. The total acidity of 15-Fe_3O_4@SPAN-9/3 catalyst (3.24 NH_3 mmol/g) is also markedly higher than those of Fe_3O_4 (2.85 NH_3 mmol/g) and PANI (0.19 NH_3 mmol/g). Although the NH_3-TPD analysis does not specify the kinds (Lewis or Brønsted) of acidic sites in the catalyst, it may be inferred that the introduction of a sulfate group might enhance the concentration of Brønsted acid sites based on the evidence of a few previously published studies [41].

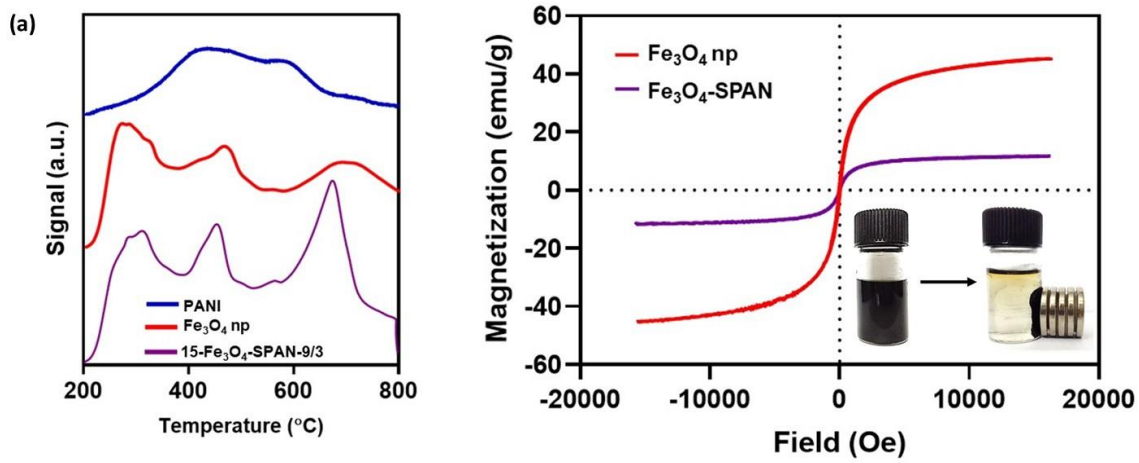

Fig. 5.6. *NH_3-TPD analysis of the synthesized catalysts (a), and VSM magnetization curves of Fe_3O_4 nanoparticles and 15- Fe_3O_4@SPAN-9/3 catalyst (b).*

Table 5.1. *Total acidity of PANI, Fe_3O_4 nanoparticles, and 15- Fe_3O_4@SPAN-9/3 catalyst.*

	Total acidity (NH_3 mmol/g)			
Sample	Weak	Moderate	Strong	Total
PANI	0	0.19	0	0.19
Fe_3O_4 np	0.90	0.97	0.98	2.85
15-Fe_3O_4@SPAN-9/3	0.90	0.73	1.61	3.24

The VSM results of pure Fe_3O_4 nanoparticles and 15- Fe_3O_4@SPAN-9/3 catalyst are presented in Fig. 5.6 b and Table 5.2. The results revealed that both the samples have negligible coercivity (Hc) and remanent magnetization (M_r) in the absence of an external magnetic field that confirms their superparamagnetic nature at room temperature [42]. 15-Fe_3O_4@SPAN-9/3 showed lower M_r and Hc values compared to pure Fe_3O_4 nanoparticles. This could be attributed to the functionalized polyaniline matrix present in 15-Fe_3O_4@SPAN-9/3 that reduces the superparamagnetic behaviour of the catalyst. The saturation magnetization (M_s) of pure Fe_3O_4 nanoparticles and 15- Fe_3O_4@SPAN-9/3 is 45.6 and 37.3 emu/g respectively. The superparamagnetic property is an excellent property for aiding the magnetic recovery of the catalyst from the reaction mixture, allowing for recyclability and reuse.

Table 5.2. *Magnetic parameters of Fe_3O_4 nanoparticles and 15-Fe_3O_4@SPAN-9/3 catalyst.*

Sample	M_s (emu/g)[a]	Hc (Oe)[b]	M_r (emu/g)[c]
Fe_3O_4 np	45.6	0.18	0.003
15-Fe_3O_4@SPAN-9/3	37.3	4.91	0.024

[a]Saturation magnetization, [b]Coercivity, [c]Remanent magnetization

In order to confirm the formation of 15-Fe_3O_4@SPAN-9/3 catalyst, the XPS technique was employed to gain insight into the surface chemical states. The wide-scan survey spectra of 15-Fe_3O_4@SPAN-9/3 (Fig. 5.7 a) show the distinct peaks at binding energies 710.80, 530.23, 398.72, 283.63, and 167.62 eV that are assigned to Fe(2p), O(1s), N(1s), C(1s) and S(2p), respectively. Two prominent binding energy peaks at 711.37 and 724.97 eV were observed in the deconvoluted scan of Fe(2p) (Fig. 5.7 b) that corresponds to the electronic states of Fe $2p_{3/2}$ and Fe $2p_{1/2}$, respectively [43]. These two peaks are characteristic of Fe^{2+} and Fe^{3+} and a satellite peak situated at around 719.79 eV is observed which is a typical peak of Fe^{3+} in γ-Fe_2O_3 indicating that the surface of Fe_3O_4 is partially oxidized. Furthermore, the Fe^{3+}/Fe^{2+} ratio calculated from the peak area is found to be 2.12, which is close to 2:1 in Fe_3O_4 [44, 45]. The deconvoluted scan of C(1s) (Fig. 5.7 c) shows the presence of benzene ring-C C-N/C=N (284.67 eV), (C-C/C-H, 284.80 eV), and C=O of quinoid (285.89 eV). The N(1s) peak is deconvoluted into four peaks (Fig. 5.7 d) related to benzenoid-amine constituent (-NH-) (399.89 eV), quinoid-imine (=NH-) (399.74 eV), nitrogen atom with a delocalized positive charge ($-N^+$) (399.00 eV) and positively charged nitrogen ($-NH^+-$) (401.20 eV) [46]. The deconvolution of the O(1s) peak, as shown in Fig. 5.7 e, resulted in three peaks at binding energies 531.40, 531.18, and 532.60 eV that corresponds to lattice oxygen, OH-group, and molecular water present in the sample. The results are consistent with the previously reported values [47]. The two binding energy peaks at 168.44 and 169.75 eV in the deconvoluted scan of S(2p) (Fig. 5.7 f) are ascribed to $-SO_3^-$ and $-SO_3H$ groups [48], respectively that further confirming the successful sulfate functionalization of the catalyst.

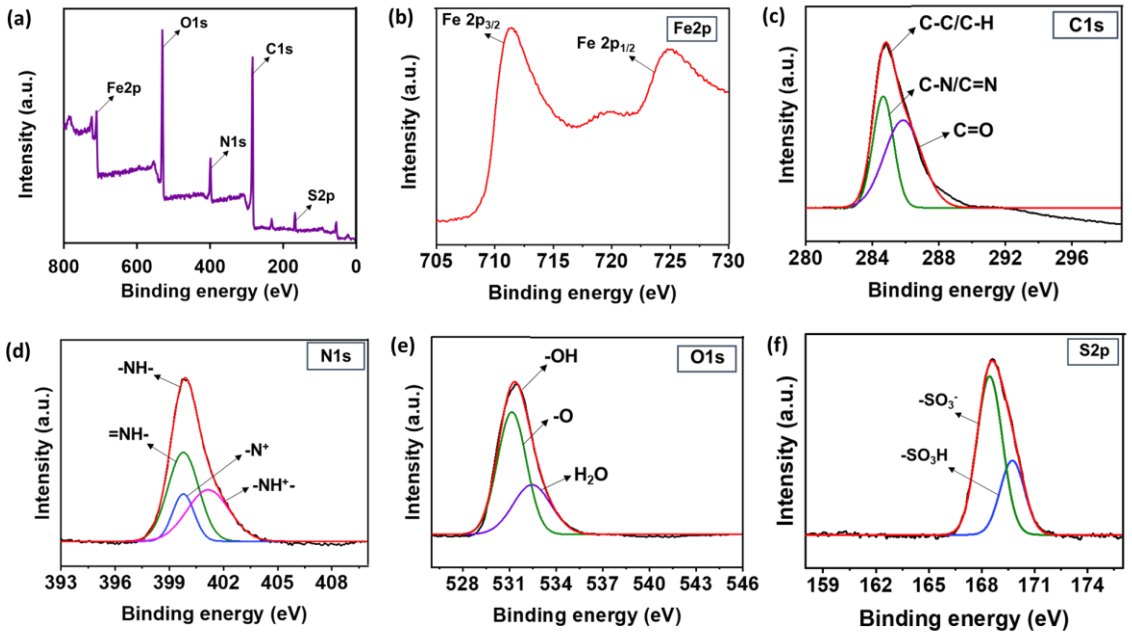

Fig. 5.7. *XPS survey scan of 15-Fe_3O_4@SPAN-9/3 (a); high resolution XPS spectra of Fe(2p) (b), C(1s) (c), N(1s) (d), O(1s) (e), and S(2p) (f).*

Fig. 5.8 (a-c) shows the SEM micrographs of PANI, Fe_3O_4, and 15-Fe_3O_4@SPAN-9/3 catalysts. The image of PANI shows the well-grown interconnected fibers that are porous in surface morphology Fig. 5.8 a. Fig. 5.8 b shows Fe_3O_4 nanoparticles which have nearly spherical morphology. From Fig. 5.8 c it is evident that in 15-Fe_3O_4@SPAN-9/3 nanocomposite the spherical Fe_3O_4 nanoparticles are embedded within the net-like structure of PANI fibers and due to sulfonation the structure of the cylindrical fibers is slightly damaged. The EDX spectrum shown in Fig. 5.8 d confirms the existence of C, N, O, Fe, and S as elemental constituents in 15-Fe_3O_4@SPAN-9/3 nanocomposite with an estimated weight percentage of 44.75%, 11.79%, 27.57%, 11.76%, and 4.13%, respectively (Fig. 5.8 d inset). Moreover, the elemental mapping analysis for C, N, O, Fe, and S (Fig. 5.8 e-i) of the 15-Fe_3O_4@SPAN-9/3 nanocomposite shows a homogeneous distribution of the elements across the examined region.

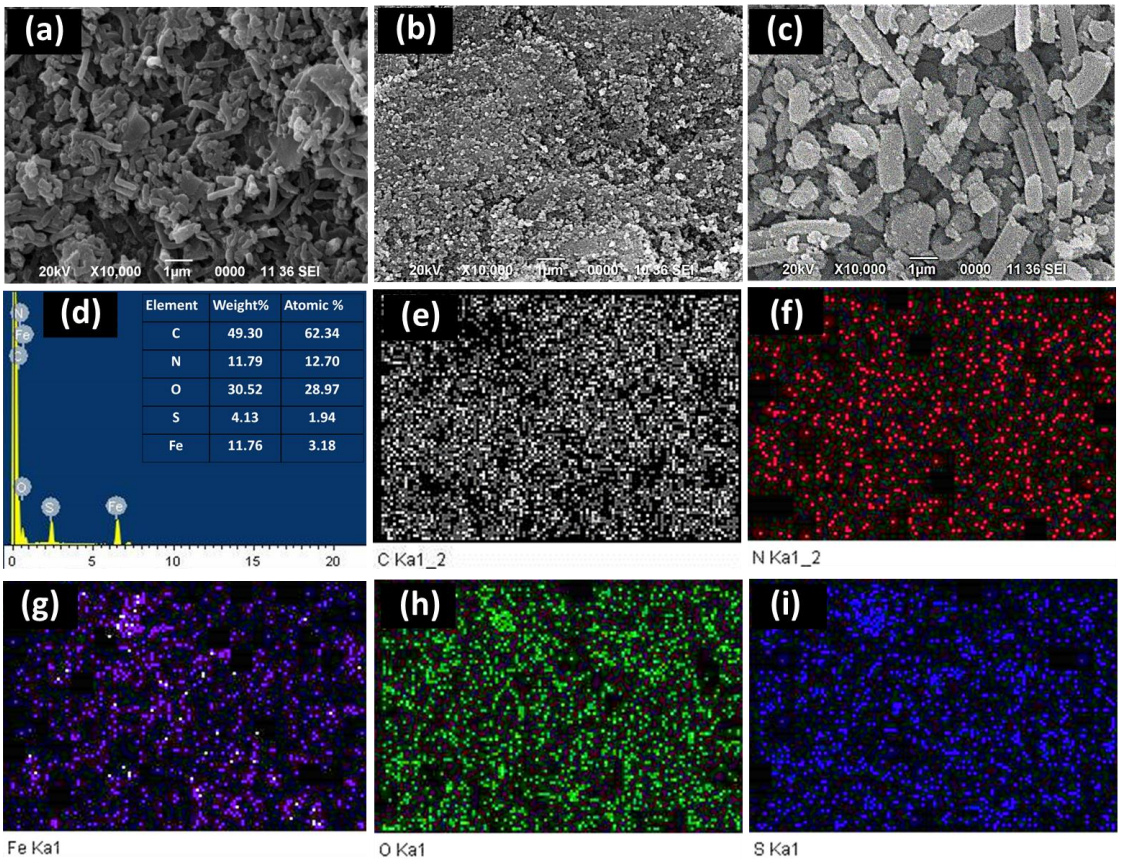

Fig. 5.8. *SEM micrographs of PANI (a), Fe_3O_4 (b), and 15-Fe_3O_4 @SPAN-9/3 (c); EDX spectrum of 15-Fe_3O_4@SPAN-9/3 (d); elemental distribution table (d inset); and pseudo-colour elemental distribution maps of 15-Fe_3O_4@SPAN-9/3 (e-i).*

The morphology of the synthesized 15-Fe_3O_4@SPAN-9/3 was characterized by TEM and HRTEM analyses. From the low magnification TEM images (Fig. 5.9 a-b) it can be seen that the sphere-like structures of Fe_3O_4 are homogenously distributed on the PANI matrix. At higher magnification (Fig. 5.9 c inset), the presence of quasi-spherical Fe_3O_4 nanoparticle is clearly observed and as calculated from the TEM micrographs, the average size of the Fe_3O_4 nanoparticle was found to be ~23.7 nm. The HRTEM image in Fig. 5.9 d shows clear lattice fringes with d-spacing of ~0.247 nm that is attributed to the (311) plane of 15-Fe_3O_4@SPAN-9/3. Fig. 5.9 e shows the selected area electron diffraction (SAED) pattern depicting characteristic diffraction signatures of Fe_3O_4 nanoparticle corresponding to 311, 400, 511, and 440 diffraction planes. This also established the polycrystalline nature of the synthesized 15-Fe_3O_4@SPAN-9/3. Furthermore, the particle size and distribution were assessed using Image J software and shown in a histogram, as shown in Fig. 5.9 f. The majority of metallic particles are 10-50 nm in size, with an average

size of 23.7 nm. All the results obtained from TEM analysis are also corroborated with the p-XRD data as discussed earlier.

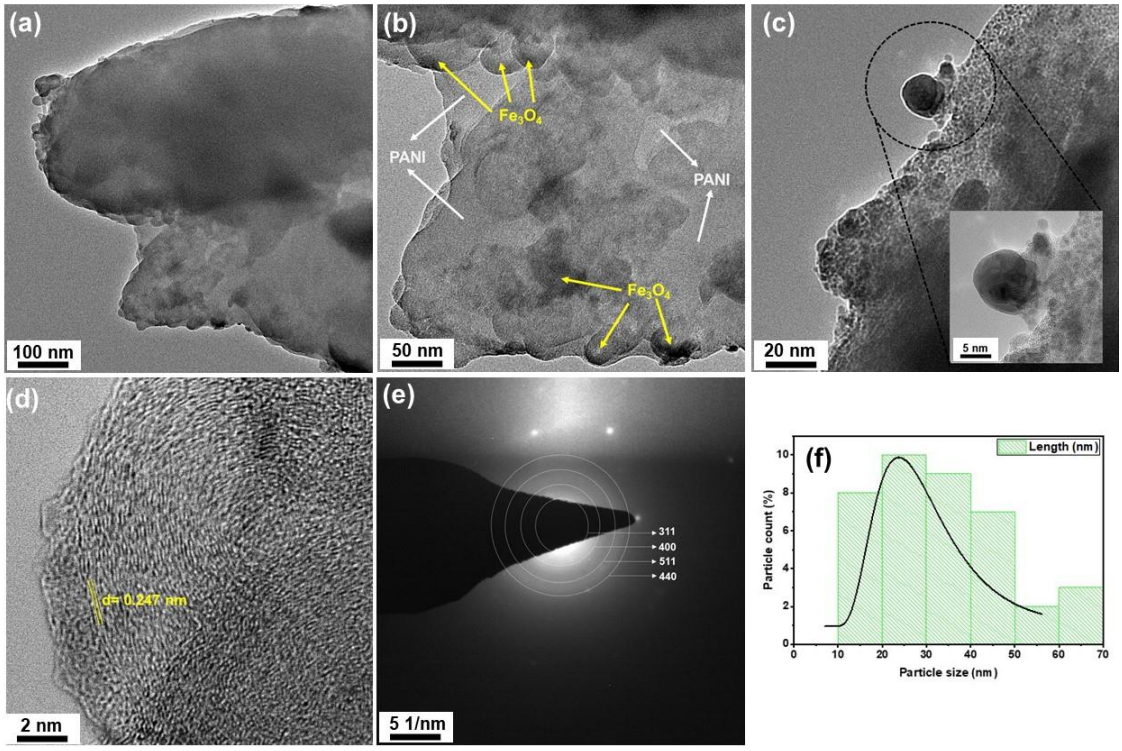

Fig. 5.9. *Low magnification TEM images (a, b), HRTEM image (c, d), the SAED pattern (e), and the corresponding particle size distribution for 15-Fe_3O_4@SPAN-9/3 (f). The white and yellow arrows in (b) show the existence of PANI and Fe_3O_4 nanoparticles.*

The porous nature and specific surface area of the samples were investigated by measuring nitrogen adsorption-desorption isotherms and are shown in Fig. 5.10. In order to show the effect of sulfate functionalization on polyaniline fibers we have also studied the adsorption-desorption isotherm of SPAN. It is seen from Fig. 5.10 a and Fig. 5.10 b that both PANI and SPAN exhibit type II isotherms according to the IUPAC classification, which is in accordance with macroporous material [49]. The isotherms also display a hysteresis loop at higher relative pressures (P/P_0 close to 1), which is normally associated with capillary condensation within mesopores, confirming the presence of textural mesoporosity within the matrix. The slight increase in surface area of SPAN from 33.95 m^2g^{-1} to 35.63 m^2g^{-1} is due to the functionalization of -SO_3H groups on the PANI surface. Also, the corresponding pore size distribution curve computed from the desorption branch of the nitrogen isotherm using the BJH (Barrett-Joyner-Halenda) technique of PANI and SPAN was inhomogeneous, as shown in the insets of Fig. 5.10 a and Fig. 5.10 b. The BET surface area, average pore size, and pore volume of all the samples are provided in Table

5.3. The nitrogen adsorption-desorption isotherms of Fe_3O_4 nanoparticle (Fig. 5.10 c) and 15-Fe_3O_4@SPAN-9/3 (Fig. 5.10 d) can be classified as type IV isotherms which is characteristic of mesoporous solids with pore diameters between 2-50 nm [50]. The corresponding pore size distribution curves, as shown in the insets of Fig. 5.10 c and Fig. 5.10 d and the data (Table 5.3) demonstrate that 15-Fe_3O_4@SPAN-9/3 has a lower BET surface area (145.93 m^2g^{-1}) and smaller pore (2.6 nm) compared to pure Fe_3O_4 (172 m^2g^{-1} and 3.1nm). It is believed that the PANI matrix grafted with -SO_3H groups caused the closing of some pores and resulted in a reduced surface area and smaller pore size of 15-Fe_3O_4@SPAN-9/3.

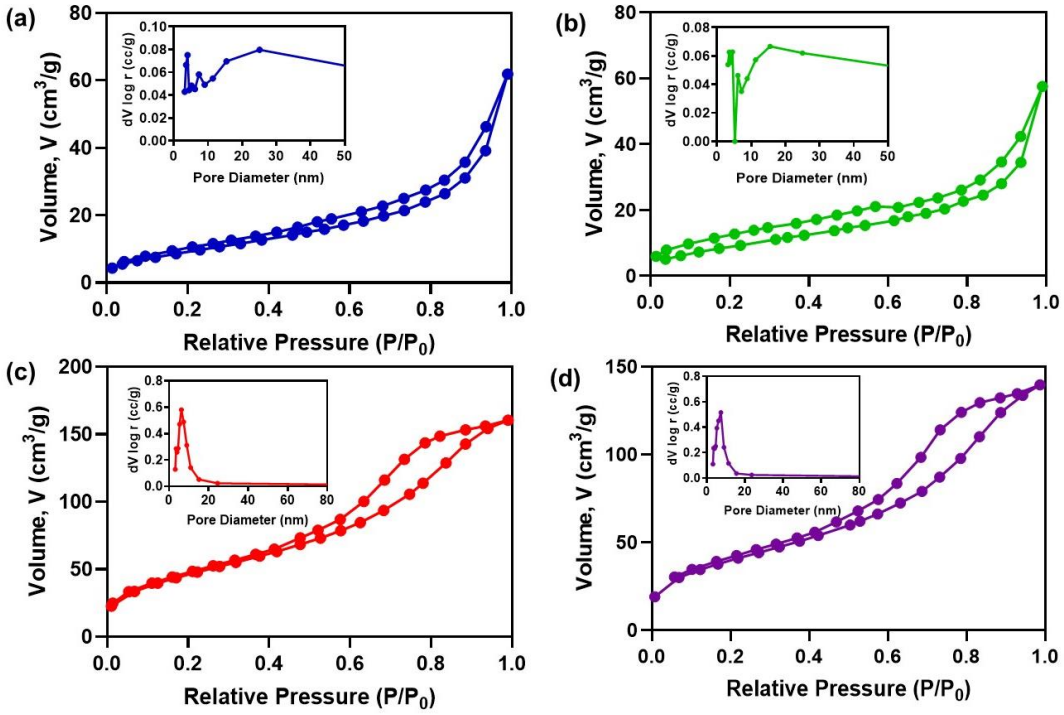

Fig. 5.10. *Nitrogen adsorption-desorption isotherms and the corresponding pore size distribution curves (insets) of PANI (a), SPAN (b), Fe_3O_4 (c), and 15-Fe_3O_4@SPAN-9/3 (d).*

Table 5.3. *BET analysis data of the different catalysts.*

Catalyst	BET Surface area (m^2g^{-1})	Average pore size (nm)	Total pore volume (cm^3g^{-1})
PANI	34	1.9	0.079
SPAN	36	1.8	0.089
Fe_3O_4 np	172	3.1	0.225
15-Fe_3O_4@SPAN-9/3	145.93	2.6	0.196

5.3.3. Optimization of reaction parameters for HMF production using Multivariable Experimental Design

RSM for modelling and optimization:

The optimal values of the experimental factors and the effect of their interactions on HMF yield were determined using CCD-based RSM. In our study, the reaction parameters considered were temperature, reaction time, catalyst loading, and substrate concentration within well-defined boundary conditions with a 95% confidence limit, as shown in Table 5.4. Thus, for optimization of glucose-to-HMF conversion reaction a five level-four factor (5^4) CCD has been applied that generates 21 sets of reaction conditions. The results obtained corresponding to each experimental run are given in Table 5.5. The following equation represents the empirical relationships between the four variables and the HMF yield by 15-Fe_3O_4@SPAN-9/3:

HMF yield (%) = +73.56 - 0.28 * A +10.9 * B +2.62 * C - 1.13 * D +6.66 * A * D
+ 2.84 *B * C - 1.95 * B * D - 2.57 * A^2 - 12.65 * B^2 - 2.80 * C^2 - 2.46 * D^2

where, A = temperature (°C), B = reaction time (h), C = catalyst loading (mg) and D = substrate concentration (mMol).

Table 5.4. *Coded levels of variables for CCD Response Surface Methodology.*

Variables	Units	Coded Levels				
		-α	-1	0	1	+α
(A) Temperature	°C	120	135	150	165	180
(B) Reaction time	h	0	2	4	6	8
(C) Catalyst loading	mg	20	30	40	50	60
(D) Substrate concentration	mMol	40	60	80	100	120

The experimental findings corroborated well the predicted outcomes of the reaction conditions. Analysis of variance (ANOVA) as shown in Table 5.6 was used to assess statistical significance, fit competence, and anticipated model competency. As a result, the determination coefficient (R^2) was assumed to have a high degree of perfect fit. The expected R^2=0.97 remained in close agreement with the predicted R^2=0.72, indicating that the model was acceptable. This also suggests that 97% of the total variations in the reaction

parameters could be explained by the RSM prediction model. Further, the sufficient precision of 50, which is significantly higher than the normal precision value of 4, demonstrates that the quadratic model may be used to evaluate the variation in reaction parameters with high accuracy [51].

Table 5.5. *CCD and ANN matrix for the four independent variables on the HMF yield with the predicted and actual response.*

Experimental runs	Temperature (°C)	Reaction time (h)	Catalyst (mg)	Substrate (mMol)	HMF Yield%					
					RSM			ANN		
					Predicted	Observed	Residuals	Predicted	Observed	Residuals
1	135	6	30	100	49.06	49.97	-0.91	50.50	51.03	0.53
2	165	6	30	60	54.65	55.94	-1.29	55.94	55.94	0.00
3	150	4	40	80	73.56	73.78	-0.22	73.16	72.53	-0.63
4	150	4	20	80	57.10	56.04	1.06	56.04	56.04	0.00
5	150	4	40	80	73.56	75.17	-1.61	73.16	71.14	-2.02
6	165	2	50	100	49.13	51.04	-1.91	51.04	51.04	0.00
7	165	2	30	100	49.58	49.42	0.16	49.42	49.42	0.00
8	150	4	40	120	61.45	60.84	0.61	61.11	61.39	0.27
9	135	6	50	100	59.98	60.82	-0.84	60.82	60.82	0.00
10	135	2	30	60	48.51	50.87	-2.36	50.87	50.87	0.00
11	150	4	60	80	67.58	66.36	1.22	68.58	70.79	2.22
12	150	4	40	80	73.56	73.75	-0.19	73.16	72.56	-0.59
13	120	4	40	80	63.82	62.68	1.14	62.55	62.41	-0.13
14	135	2	50	60	48.06	48.52	-0.46	48.52	48.52	0.00
15	150	4	40	80	73.56	73.54	0.02	73.16	72.77	-0.39
16	180	4	40	80	62.70	61.56	1.14	61.56	61.56	0.00
17	150	4	40	40	65.97	64.29	1.68	64.29	64.29	0.00
18	150	8	40	80	44.78	43.64	1.14	43.64	43.64	0.00
19	150	4	40	80	73.56	71.55	2.01	73.16	74.76	1.61
20	150	0	40	80	1.14	0	1.14	2.43	4.87	2.43
21	165	6	50	60	65.57	67.1	-1.53	67.10	67.10	0.00

The fitted model obtained p-values in the ≤ 0.0001 range, indicating that its confidence levels were adequate. For the analysis, an α-value of 0.05 was chosen, which corresponds to a 95% confidence level. The p-values for the fitted models were found to be smaller than the α-value, indicating that the null hypothesis was rejected and the statistical significance of the fitted model was confirmed. Furthermore, the fitted models

had high F-values whereas the values indicating lack of fit were non-significant, validating the goodness of fit (Table 5.6). While estimating the HMF yield with change in reaction parameters, a p-value < 0.05 suggests that the variable is highly significant, whereas a p-value > 0.1 suggests that the variable is insignificant [52]. For glucose-to-HMF reaction, the variation of temperature, reaction time, catalyst loading, and substrate concentration in the reaction, significantly influenced the HMF yield, in the fitted single factor interactions (Figs. 5.11 a-d). On the other hand, AD, BC, BD, A^2, C^2, B^2, and D^2 are quadratic relationships that have a significant influence on the HMF yield (Table 5.6). Single factor interaction plots as shown in Figs. 5.11 a-d, are used to study the effect of interaction among the significant parameters. Likewise, Figs. 5.11 e-g and e'-g' show relevant multivariate 3D interaction plots and their accompanying contour plots. In the case of single-factor interactions, the impact of reaction time is seen to be highly significant as compared to other reaction parameters. From Figs. 5.11 b, it is seen that increasing reaction time results in an improvement of the HMF production initially, reaching a maximum yield and then decreasing the yield with further increase in time. Similarly, an increase in the loading of catalysts also increases the yield of HMF (Figs. 5.11 c). On the other hand, temperature and substrate concentration have a negligible effect on HMF production when introduced within the boundary limits (Figs. 5.11 a, d).

Table 5.6. *ANOVA for the fitted quadratic polynomial model for HMF yield.*

Source	Sum of Squares	Degree of Freedom	Mean Square	F value	p-value Prob > F	
Model	5332.59898	11	484.7817255	133.3695268	< 0.0001	S*
A-Temperature	0.6272	1	0.6272	0.172550579	0.6876	NS#
B-Reaction time	952.2248	1	952.2248	261.9689735	< 0.0001	S
C-Catalyst	109.8304	1	109.8304	30.21571917	0.0004	S
D-Substrate	20.4304	1	20.4304	5.620659025	0.0419	
AD	177.555625	1	177.555625	48.84777714	< 0.0001	S
BC	64.63845	1	64.63845	17.78284749	0.0022	S
BD	15.1321	1	15.1321	4.163030309	0.0717	
A^2	166.2904941	1	166.2904941	45.7485985	< 0.0001	S
B^2	4015.635867	1	4015.635867	1104.751741	< 0.0001	S
C^2	197.3356236	1	197.3356236	54.28950258	< 0.0001	S
D^2	152.2269236	1	152.2269236	41.87953402	0.0001	S
Residual	32.71388625	9	3.63487625			
Lack of Fit	25.99680625	5	5.19936125	3.096203261	0.1481	NS
Pure Error	6.71708	4	1.67927			
Cor Total	5365.312867	20				
Std. Dev. = 1.91		**Mean = 57.95**		**Predicted R^2 = 0.72**		
R^2 = 0.97		**Adj. R^2 = 0.96**		**Adequate Precision = 50.25**		

*Significant; #Non-significant

The response surface 3D graphs showing the influence of bivariate interactions of 15-Fe_3O_4@SPAN-9/3 catalyst on glucose-to-HMF reaction are shown in Figs. 5.11 e-g. As evident from the response plot shown in Fig. 12 e reaction temperature was able to influence the HMF production in association with substrate concentration. Reaction time, on the other hand, influences the HMF yield, when in conjunction with either catalyst loading (Fig. 5.11 f) or substrate concentration (Fig. 5.11 g). Thus, the reaction time was shown to have the highest significant impact on the glucose-to-HMF reaction, as shown by the single factor interaction plot (Fig. 5.11 b) and response surface plot (Fig. 5.11 f and g). A maximum HMF yield of 75.17% was observed for this univariate and bivariate interaction using 40 mg of the catalyst with 80 mMol of glucose at 150°C for 4h. Similarly, a maximum HMF yield of 73.78% was achieved using 80 mMol of glucose at 150°C signifying the interactions between substrate concentration and reaction temperature.

The contour maps for the preceding 3D graphs (Fig. 5.11 e-g) are shown in Figs. 5.11 e′-g′. An elliptical contour map suggests that the interactions between the respective variables are substantial, whereas a circular contour plot indicates that the interactions are

trivial. As evident from Figs. 5.11 é-ǵ, the contour plots for the fitted model are elliptical, indicating that the variables interact significantly [53].

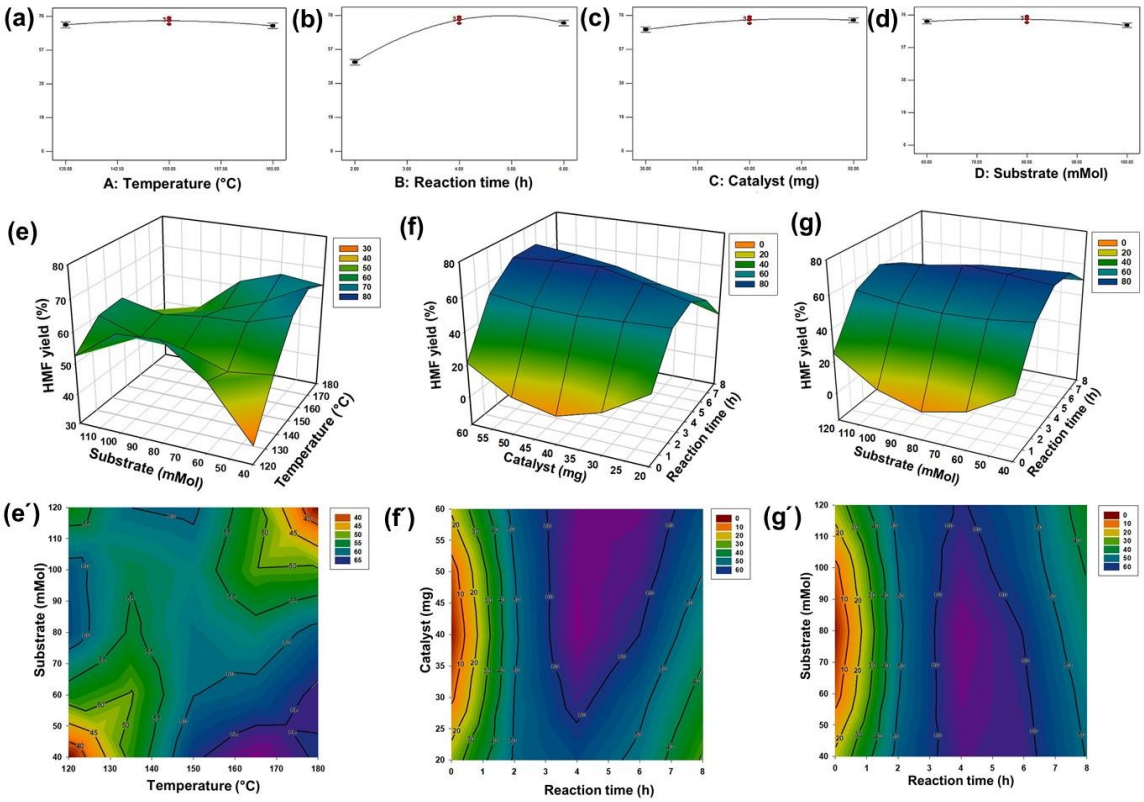

Fig. 5.11. *Effect of univariate interactions defined by the CCD-RSM model on the HMF yield (a-d); effect of multivariate interactions: response surface 3D plots (e-g) and the corresponding contour plots (e´-g´) defined by the CCD-RSM model on the HMF yield.*

To assess the adequacy of the model, a normal probability plot was used to analyse the standard deviation between the expected and experimental results. Fig. 5.12 a depicts an almost linear distribution of data points creating a straight line, which is consistent with the normally distributed residuals of the response. Fig. 5.12 b represents the similarity between the predicted and actual values. Furthermore, Pareto graphic analysis (Fig. 5.12 c) was used to establish the percentage influence of the most relevant parameters, with reaction time being shown to be the most significant factor, which is consistent with the results obtained (Table 5.7).

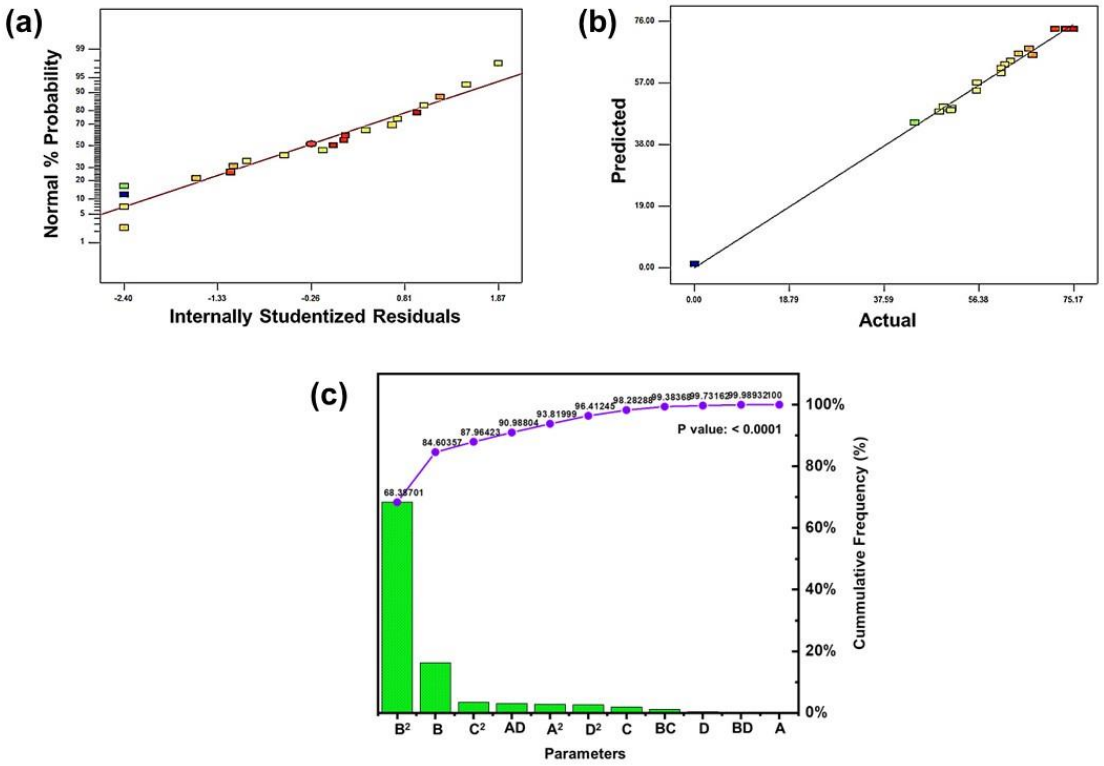

Fig. 5.12. *Normal probability plot (a), predicted vs. actual plot (b), and Pareto graphic analysis described by the model.*

ANN for modelling and optimization:

The dataset derived from RSM has been used to build and train the neural network using 21 data points. The network is trained with 80% of the entire experimental data, with the remaining data utilized for model testing and validation. Prior to the training session, the inputs and targets are normalized to prevent overflow situations. This neural network was trained using the LM back propagation approach, which employs second-degree derivatives of mean squared error (MSE). The network training is required to halt when the error of the network reduces considerably to a low value (MSE $\leq E_o$, where the objective E_o is set at 5×10^{-4}). The training in the current study ended after 6 iterations (epochs). The progression of the MSE of the neural network throughout the training period is depicted in Fig. 5.13 a. As seen from Fig. 5.13 a, the last point of the training data has a performance function MSE less than the predefined target, suggesting that network training was effective. Further, the plot (Fig. 5.13 a) indicates that the test set error and the validation mean square error have comparable features with a minimal MSE and no over-fitting.

Table 5.7. *Statistical error functions.*

Error function	Equation	Reference
Root mean square error	$\text{RMSE} = \sqrt{\frac{1}{N}\sum_{i=1}^{N}\left(\frac{P_{R,\exp(i)}-P_{R,cal(i)}}{P_{R,\exp(i)}}\right)^2}$	[24]
Hybrid fractional error function	$\text{HYBRID (\%)} = \frac{1}{N-P}\sum\left[\frac{\left(P_{R,i,exp}-P_{R,i,cal}\right)^2}{P_{R,i,exp}}\right]100$	[54]
Average relative error	$\text{ARE (\%)} = \frac{100}{N}\sum_{i-1}^{N}\frac{\left\|P_{R,i,exp}-P_{R,i,cal}\right\|}{P_{R,i,exp}}$	[24]
Absolute average relative error	$\text{AARE} = \frac{1}{N}\sum_{i=1}^{N}\left(\left\|\frac{P_{R,\exp(i)}-P_{R,cal(i)}}{P_{R,\exp(i)}}\right\|\right)$	[54]
Marquardt's percent standard error deviation	$\text{MPSED (\%)} = \sqrt{\frac{\sum\left(\frac{P_{R,exp}-P_{R,cal}}{P_{R,exp}}\right)^2}{N-P}}\times 100$	[24]
Correlation coefficient	$R^2 = \frac{\sum_{i=1}^{N}\left(P_{R,i,cal}-P_{R,exp,ave}\right)^2}{\sum_{i=1}^{N}\left(P_{R,i,cal}-P_{R,exp,ave}\right)^2+\sum_{i=1}^{N}\left(P_{R,i,cal}-P_{R,i,exp}\right)^2}$	[55]
Adjusted R^2	$\text{Adj } R^2 = 1-\left[(1-R^2)\times\frac{N-1}{N-P-2}\right]$	[24]

where N is the number of experimental runs; $P_{R,exp(i)}$, $P_{R,i,exp}$ are the experimental values of the i^{th} experiment; $P_{R,\,cal(i)}$, $P_{R,i,\,cal}$ are the model predictions of the i^{th} experiment; $P_{R,exp,\,ave}$ is the experimentally determined average value, N is the number of experimental runs while P is the number of factors.

The regression curve of the proposed model is presented in Fig. 5.13 b, and the associated values for training, testing, validation, and total data were 0.9988, 0.9885, 0.9998, and 0.9987, respectively. The correlation coefficients were ~1 in all data sets, indicating that the fit was appropriate for all data sets. Furthermore, the fit line for the training and total data sets was on the 45-degree line, indicating that the targets were almost comparable to the network outputs. As a result, the ANN output network response regarding the HMF yield prediction accuracy was adequate [24]. Table 5.5 shows the overall ANN expected HMF yield based on each reaction condition and the evaluation using the investigational data set.

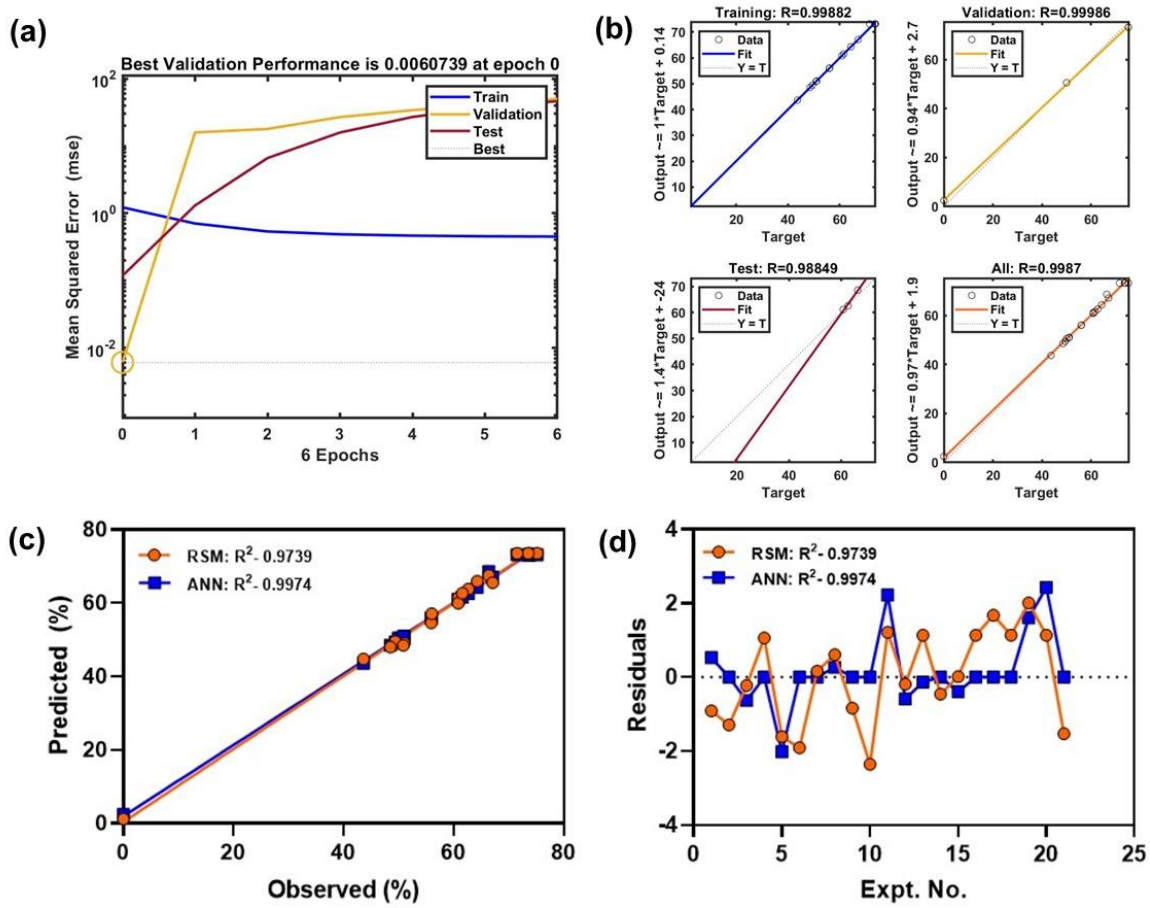

Fig. 5.13. *Selection of the best ANN architecture based on mean squared error (MSE) values (a) and the determination coefficients (R^2) (b); comparison of the predictive outputs of RSM and ANN models based on determination coefficients (c) and distribution of residuals (d).*

Comparison of the RSM and ANN models:

The prediction outputs of the two models, as well as the experimental results, are shown in Table 5.5. Their performance was assessed using linear correlation plots and residual distribution graphs, as illustrated in Figs. 5.13 c, d. The linear correlation plots with high R^2 values (>0.9) are shown in Figs. 5.13 c indicates that both RSM and ANN models agreed well with the experimental data (Table 5.5). This validates the use of both RSM and ANN prediction models for optimizing reaction parameters for HMF synthesis. Additionally, the higher R^2 value of the ANN model and the localization of their residual quantities near the centre line (Figs. 5.13 d) implies that the ANN model's prediction was more appropriate in estimating the HMF yield than the RSM model. However, ANN-based models lack the capacity to use mathematical frameworks to explain the influence of experimental factors on actual output based on comparative significance/insignificance,

which is a distinguishing feature of RSM-based prediction models [56]. Thus, in the current work, the combined usage of RSM and ANN prediction models was discovered to be critical in identifying the major influence of experimental factors on HMF production with better approximation and generalization capacities for predictive evaluations.

Furthermore, to analyse the accuracy of the model's prediction, seven statistical error functions, correlation coefficient, root mean square error (RMSE), average relative error (ARE), absolute average relative error (AARE), hybrid fractional error function (HYBRID), adjusted R^2 and Marquardt's percent standard error deviation (MPSED) were employed as presented in Table 5.8. The competence of the model to predict was evidenced by the low values of the error functions. Both models had minimal error levels, according to the results. R^2 and adjusted R^2 were also calculated. To explore the overestimation of R^2, adjusted R^2 was utilized, and the values obtained for both models were reasonably high, confirming their significance. The higher the R^2 and adjusted R^2 values, the more reliable the model predictions. Overall, the statistical data showed that the ANN model performed slightly better than the RSM model.

Table 5.8. *Statistical error indices of RSM and ANN.*

Error function	**Results**	
	RSM	**ANN**
RMSE	0.016	0.0091
HYBRID (%)	0.7014	2.8012
ARE (%)	0.4134	1.3410
AARE	0.0200	0.0067
MPSED (%)	0.9076	2.0000
R^2	0.9739	0.9934
Adj R^2	0.9616	0.9956

5.3.4. Experimental validation of RSM and ANN optimal predictive output and assessment of the catalytic performance of 15-Fe_3O_4@SPAN-9/3 with lignocellulose (*Saccharum spontaneum* and banana peduncle) derived glucose

RSM and ANN's best prediction outputs were further confirmed experimentally by executing conversion reactions under ideal conditions (Experimental run 5, Table 5.5). The experimental findings indicated 100% glucose conversion and 74.32% and 74.79% HMF yield, which were quite near to our predicted values (Table 5.9). The HMF peaks in

each condition, as well as the HMF standard curve, are displayed in the HPLC chromatogram (Fig. 5.14 a, b). The magnified view of the HPLC chromatogram (Fig. 5.14 b inset) shows no peaks of glucose or any other products, indicating 100% glucose conversion in each run with no byproducts. In fact, the estimated glucose conversion in each reaction condition was found to be > 98%, as shown in Table 5.5. Although levulinic acid and formic acid were supposed to be the main byproducts in the glucose-to-HMF reaction [7, 8], zero byproducts and 100% glucose conversion in this work, could be attributed to the fact that the catalyst acidity is not too strong to rehydrate the produced HMF and the use of DMSO/Water (4:1) as solvent. Introducing an adequate quantity of water to DMSO can promote the thermodynamic equilibrium for HMF yield from cellulosic materials, by suppressing the formation of condensation byproducts and hydration of furans produced in the reaction medium resulting in a significant increase in overall HMF production [57]. This was further confirmed by Jiang et al. that the influence of DMSO solvent on HMF yield performed the dehydration process from fructose to HMF, whereas the effect of water on HMF yield caused the isomerization reaction from glucose to fructose [58]. Thus, the synergistic effect of 15-Fe_3O_4@SPAN-9/3 catalyst and DMSO/Water solvent is likely to enhance the glucose conversion and HMF production significantly, inhibiting any condensation byproducts and hydration of HMF in the product mixture.

To validate the catalytic activity of the 15-Fe_3O_4@SPAN-9/3 catalyst for the conversion of *Saccharum spontaneum*-derived glucose and banana peduncle-derived glucose as discussed in Chapter 2, the reactions are carried out at the optimal reaction condition (80 mMol of glucose with 40 mg catalyst at 150°C for 4h) obtained from RSM model. To attain 80 mMol of glucose, 150 mg of *Saccharum spontaneum* derived cellulose and banana peduncle-derived cellulose (as discussed in Chapter 1) were subjected to enzymatic hydrolysis using 30 FPU/g of enzyme loading, 5 mg/ml of surfactant concentration and 96 h of incubation time (as discussed in Chapter 2). As anticipated, the HMF yields from *Saccharum spontaneum* derived glucose and banana peduncle derived glucose is also much higher, at 73.88% and 74.11%, respectively (Table 5.9). Further, no byproducts are observed. The HMF peak in each case are shown in Fig. 5.14 c and Fig. 5.14 d, with a magnified view of the HPLC chromatograms (Fig. 5.14 c, d insets) showing glucose peaks with < 1% concentration.

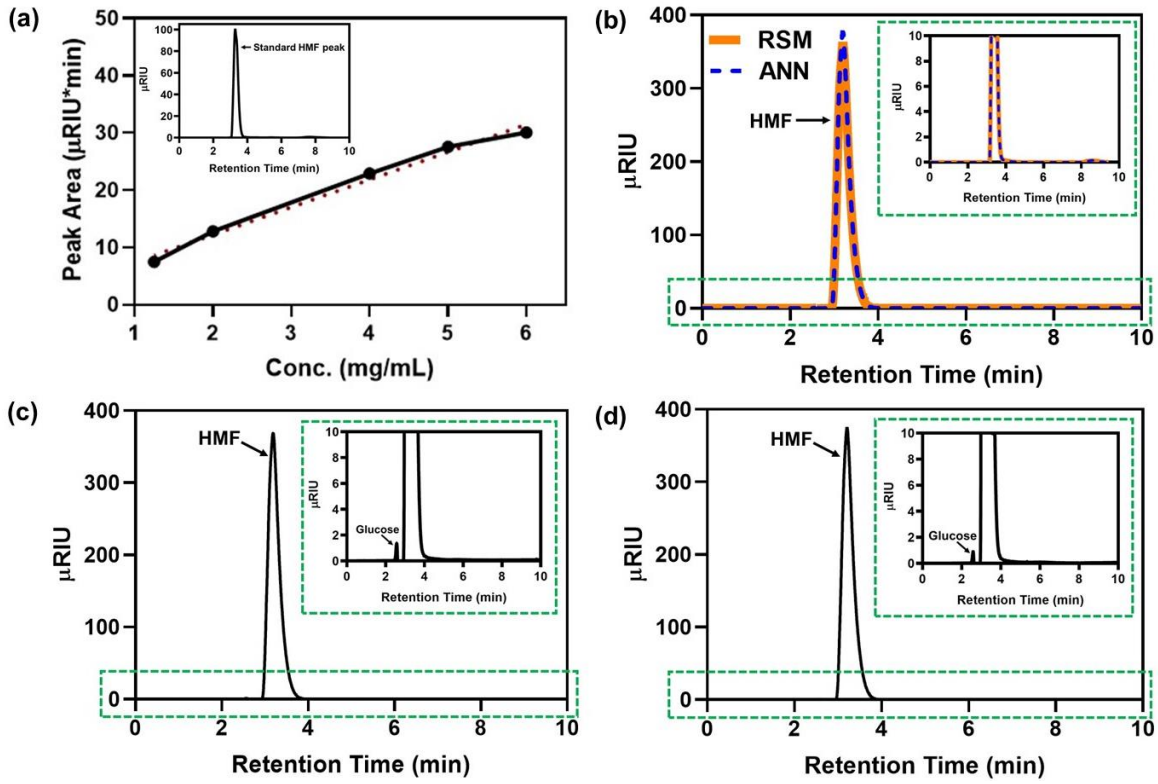

Fig. 5.14. *HMF standard curve of HPLC (a); HPLC chromatograms showing the HMF peaks at optimal conditions of RSM and ANN (b); magnified view of the HPLC chromatogram (b inset); HPLC chromatograms showing the HMF peaks from Saccharum spontaneum derived glucose (c), and banana peduncle derived glucose (d); magnified view of the HPLC chromatograms (c inset, d inset). (Reaction condition: 80 mMol glucose, 40 mg catalyst, 150°C, 4h).*

Table 5.9. *Catalytic conversion of various glucose to HMF with 15-Fe_3O_4@SPAN-9/3 catalyst. Reaction condition: 80 mMol glucose, 40 mg catalyst, 150°C, 4h.*

Substrate	Glucose conversion (%)	HMF yield (%)	HMF selectivity (%)
Standard glucose (optimal RSM condition)	100	74.32	74.32
Standard glucose (optimal ANN condition)	100	74.79	74.79
***Saccharum spontaneum* derived glucose**	99.23	73.88	74.45
Banana peduncle-derived glucose	99.11	74.11	74.78

5.3.5. Recyclability and stability of the catalyst

The recyclability performance of heterogeneous catalysts is vital for industrial applications aiming to minimize production costs. In the present study, the 15-Fe_3O_4@SPAN-9/3 catalyst was recycled and reused for five consecutive runs under the optimal conditions: 40 mg catalyst, 80 mMol of glucose, 150°C temperature, and 4h reaction time. The catalyst recovery procedure is provided in detail in section 2.7. As shown in Fig. 5.15 a, the 15-Fe_3O_4@SPAN-9/3 catalyst exhibited excellent glucose conversion that remains relatively stable at ~98-99% in all the runs. However, there is a minimal reduction in the HMF yield with 74.24% at the first use and 71.91% at the fifth use. The stability in the glucose conversion percentage in all the runs suggests that the Fe_3O_4 content in the catalyst remains constant after each recovery which is likely to act as Lewis acid for the isomerization reaction. On the other hand, the mechanism behind the reduction in HMF yield after each cyclic use was analyzed by FTIR (Fig. 5.15 b) and SEM-EDX analysis (Fig. 5.15 c) of the fresh and spent catalyst. From the SEM-EDX analysis, a minor decrease in S content in the fifth used catalyst was observed which could be due to the leaching of the weakly bound -SO_3H groups from the catalyst that led to the decrease in Brønsted acid sites in the catalyst. The constant Fe content in the fifth used catalyst was also observed in the SEM-EDX analysis. Furthermore, ICP analysis revealed that the Fe contents in the fresh and spent catalyst are approximately the same. In addition, compared to the fresh catalyst, relatively weak IR peaks related to sulfate group features were identified at 1036, 693, and 619 cm^{-1}. It suggested that the fifth used catalyst had fewer sulfate groups, which resulted in fewer Brønsted acid sites and thus a minor reduction in HMF yield. Moreover, the TGA study of spent catalyst revealed a greater weight loss than that of a fresh catalyst (Fig. 5.15 d), implying the unavoidable production and deposition of insoluble humins on the catalyst's surface, which would render the catalyst inactive for a longer time of operation.

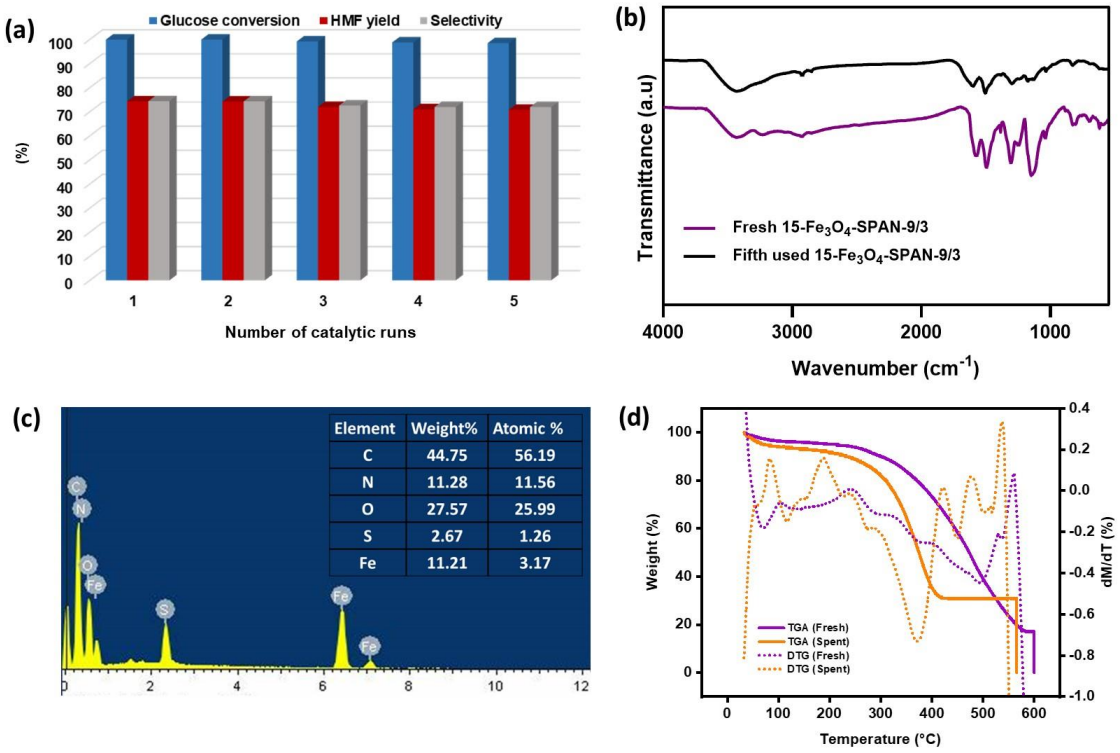

Fig. 5.15*. Catalyst recycling of 15-Fe_3O_4@SPAN-9/3 (Reaction conditions: 40 mg catalyst, 80 mMol glucose, 150°C, and 4h) (a), comparison of FTIR spectrum of 15-Fe_3O_4@SPAN-9/3 and fifth used 15-Fe_3O_4@SPAN-9/3 catalyst (b), SEM-EDX spectrum of fifth used 15 Fe_3O_4@SPAN-9/3 catalyst (c), and TGA/DTG plots of the fresh and fifth used catalyst (d).*

5.3.6. Probable mechanism for the catalytic dehydration of glucose to HMF over Fe_3O_4@SPAN-based catalyst

On the basis of earlier findings with bifunctional heterogeneous catalysts, we hypothesized that the glucose-to-HMF conversion over x-Fe_3O_4@SPAN-y/z-based catalyst would likewise involve two steps, viz., glucose isomerization to fructose followed by fructose dehydration to HMF, as depicted in Fig. 5.16. At first, Fe_3O_4, likely to provide Lewis acid sites, interacts with glucose to form fructose intermediate through three consecutive steps that consist of ring opening, isomerization, and ring-closing. Initially, deprotonation of the -OH group of C1 and subsequent protonation of the O atom of C5 would result in the ring opening of glucose. As a result, a conformational change occurs in glucose, resulting in deprotonation by Fe-O. Following that, the intramolecular shift of H from C2 to C1 causes aldose-ketose isomerization that leads to the formation of acyclic fructose, followed by conformational change and H transfer from Fe-O–H to the O of C1 to form cyclic fructose

[57, 59]. Lastly, the -SO_3H groups linked to the polyaniline surface function as Brønsted acid, driving the dehydration processes to generate HMF *via* H exchange between the catalyst and fructose, liberating three H_2O molecules [20]. The high HMF yield and selectivity obtained in this work using x-Fe_3O_4@SPAN-y/z-based catalyst can be ascribed to the well-proportioned acid types, amounts, and strength achieved through metal oxide incorporation and sulfate functionalization, as well as the optimized condition obtained from multivariate experimental design.

5.4. Comparison of the activity of 15-Fe_3O_4@SPAN-9/3 with other reported catalyst

The catalytic activity of the 15-Fe_3O_4@SPAN-9/3 catalyst for the production of HMF from glucose was compared with other reported synthetic catalysts (Table 5.10). Zhou et al. reported an HMF yield of 54.43% from glucose by $CrCl_3.6H_2O$ catalyst at 130°C and 8h in DMSO solvent [60]. The reaction time was quite high and the yield of HMF was relatively low as compared to our study. Similarly, Patrylak et al. converted glucose using zeolite as the catalyst and reported 40% HMF yield at 160°C and 4h in 100% DMSO solvent [61]. The yield of 5-HMF was somewhat low when compared to the yield obtained by the 15-Fe_3O_4@SPAN-9/3 catalyst. In another study, Hoang et al. synthesized sulfonated ZSM-5 zeolite and achieved a relatively higher yield of 54.1% HMF at 140°C and 4h in a 100% DMSO solvent [62]. Although the reaction temperature and time are almost similar to our reported study a significantly higher HMF yield (75.1 %) was observed in our reported process in a mixture of aqueous and DMSO solvent, which enhances the reactivity as well as lower the overall process cost. In addition, the catalyst we reported is bifunctional that composed of Lewis acid sites for glucose isomerization and Brønsted acid sites for fructose dehydration. As we have discussed the sulfate groups act as Brønsted acid and drive the dehydration of fructose to HMF, a high conversion yield (90%) of HMF was observed when fructose was used as substrate using a sulfonated carbon sphere as the catalyst at 160°C and 90 min in a DMSO solvent [63]. Similarly, Tomer et al. reported 74.7% HMF yield from fructose using sulfated TiO as a catalyst [64]. However, the 5-HMF synthesis from cellulose as substrate utilizing macroporous carbonaceous solid catalysts (MCSC) generated by partial hydrothermal carbonization of inorganic-organic hybrid polymers followed by sulfonation yielded a poor HMF yield of 43.1% [65]. Hence, our synthesized 15-Fe_3O_4@SPAN-9/3 catalyst could be considered a

suitable bifunctional catalyst with well-balanced Lewis-Brønsted acid sites for the efficient transformation of glucose to HMF.

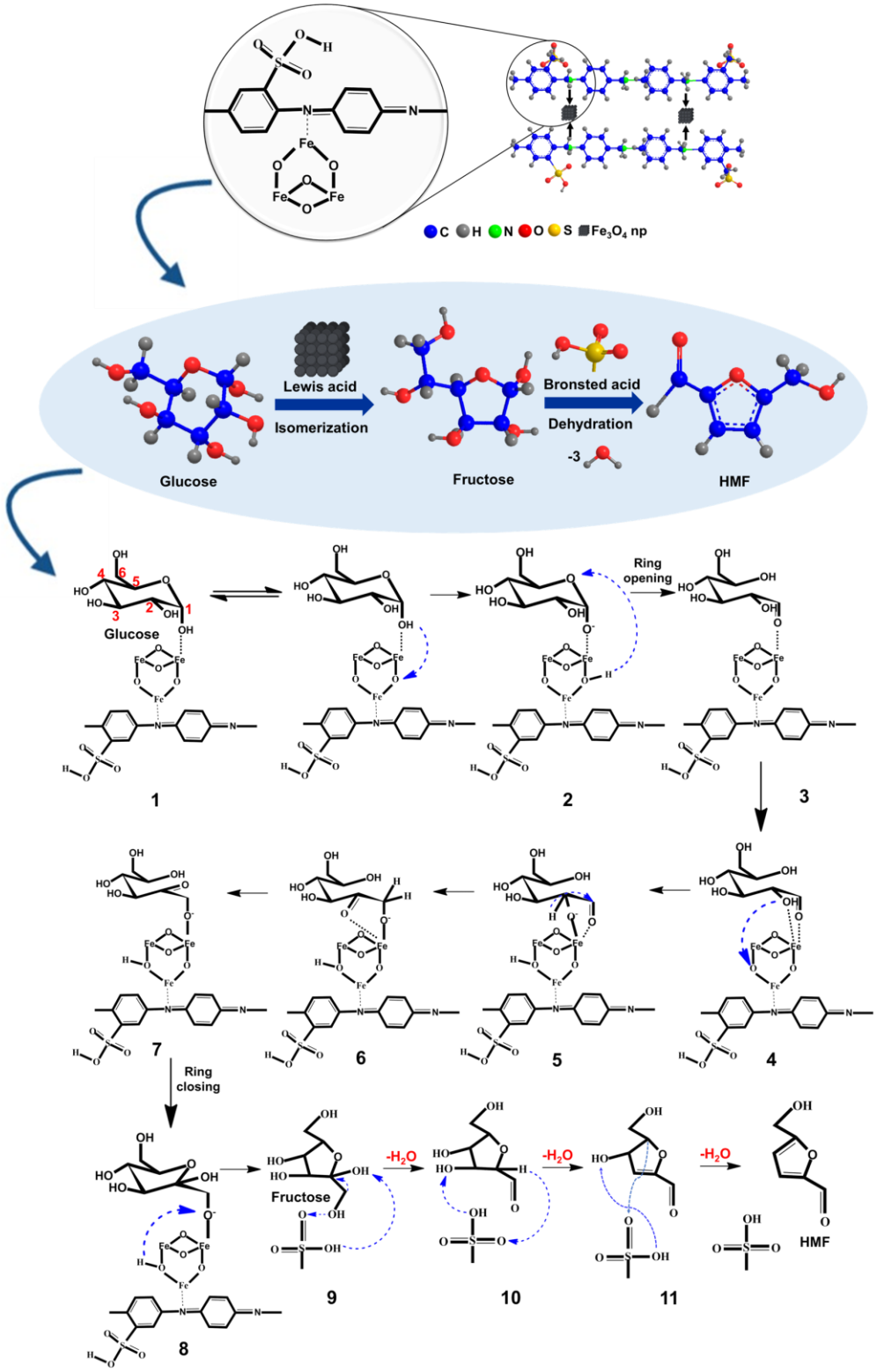

Fig. 5.16. *Mechanism proposed for the catalytic dehydration of glucose to HMF using x-Fe_3O_4@SPAN-y/z-based catalyst.*

Table 5.10. *Catalytic activity comparison of 15-Fe_3O_4@SPAN-9/3 with other reported catalysts.*

Catalyst	Substrate	Reaction temperature (°C)	Reaction Time (min)	Solvent	HMF yield (%)	Catalytic activity	Reference
$CrCl_3.6H_2O$	Glucose	130	480	DMSO	54.43	No stability study reported	[60]
Zeolite	Glucose	160	240	DMSO	40	No stability study reported	[61]
SO_3H-ZSM-5 zeolite	Glucose	140	240	DMSO	54.1	Loss of 2.2% HMF yield after fifth use	[62]
Sulfonated carbon sphere	Fructose	160	90	DMSO	90	Loss of ~15% HMF yield after fifth use	[63]
SO_4^{2-}-TiO	Fructose	150	120	DMSO	74.7	Very minimal loss in catalytic activity up to fourth use	[64]
MCSC	Cellulose	120	30	[BMIM]-Cl	43.1	Loss of 2.5% catalytic activity at fourth use	[65]
15-Fe_3O_4 @SPAN-9/3	Glucose	150	240	DMSO/H_2O	75.17	Loss of 2.3% HMF yield after fifth use	This work

5.5. Computational study on glucose conversion to HMF

The proposed mechanism described in Fig. 5.16 has been established by DFT calculations. Energy minimized electronic structures were obtained for all the species involved in the proposed reaction mechanism for the catalytic dehydration of glucose to HMF using x-Fe3O4@SPAN-y/z-based catalyst. Fig. 5.17 depicts the electronic structures of all the species optimized at the B3LYP/LANL2DZ level of theory. Bond parameters for optimal structures of glucose, Fe_3O_4, SPAN, H_2O, and HMF are provided for the complete structure, as well as selected bond parameters for other species. In the electronic structure of Fe_3O_4@SPAN, the Fe-atom of Fe_3O_4 is found to be bound to the N-atom and C-atom of SPAN at 1.985 Å and 2.381 Å distances, respectively. It was observed that after optimization the equilibrium bond length of Fe-O bond in Fe_3O_4@SPAN increases than the bond length of Fe-O in bare Fe_3O_4 species. Apart from these alterations, other bonds

in Fe_3O_4@SPAN also show increase or decrease in contrast to the equilibrium bond lengths in Fe_3O_4 and SPAN species. In structure 1, one O-atom of glucose is bonded to one Fe-atom of Fe_3O_4 at a distance of 1.949 Å. At the same time one H-atom of glucose weakly interacted with O-atom of Fe_3O_4 at a distance of 1.564 Å. It was revealed that H-atom of glucose and O-atom of $–SO_3H$ and O-atom of glucose and H-atom of $–SO_3H$ are showing weak interaction at distances of 1.824 Å and 1.636 Å, respectively. In structure 2, the distance between O-atom of glucose and Fe-atom of Fe_3O_4 was found to be 1.801 Å, while in structure 3 it was at a distance of 1.922 Å. In structure 3 it was also found that C-O bond of the glucose breaks. In structure 4, the H-atom of glucose completely relocated to the O-atom of Fe_3O_4 atom to a distance of 0.976 Å. In structure 5, Fe-atom of Fe_3O_4 formed weak interaction with two O-atoms of glucose at 1.999 Å and 2.025 Å distances and these bonds get stronger in structure 6. In structure 7, H-atom of O in Fe_3O_4 was found to be at a distance of 1.521 Å away from O-atom of glucose. Ring closure occurs in structure 8 and finally fructose is found to be generated in structure 9. Following this, fructose interacts with the $-SO_3H$ site of SPAN and coverts into HMF via three successive steps with the removal of three water molecules.

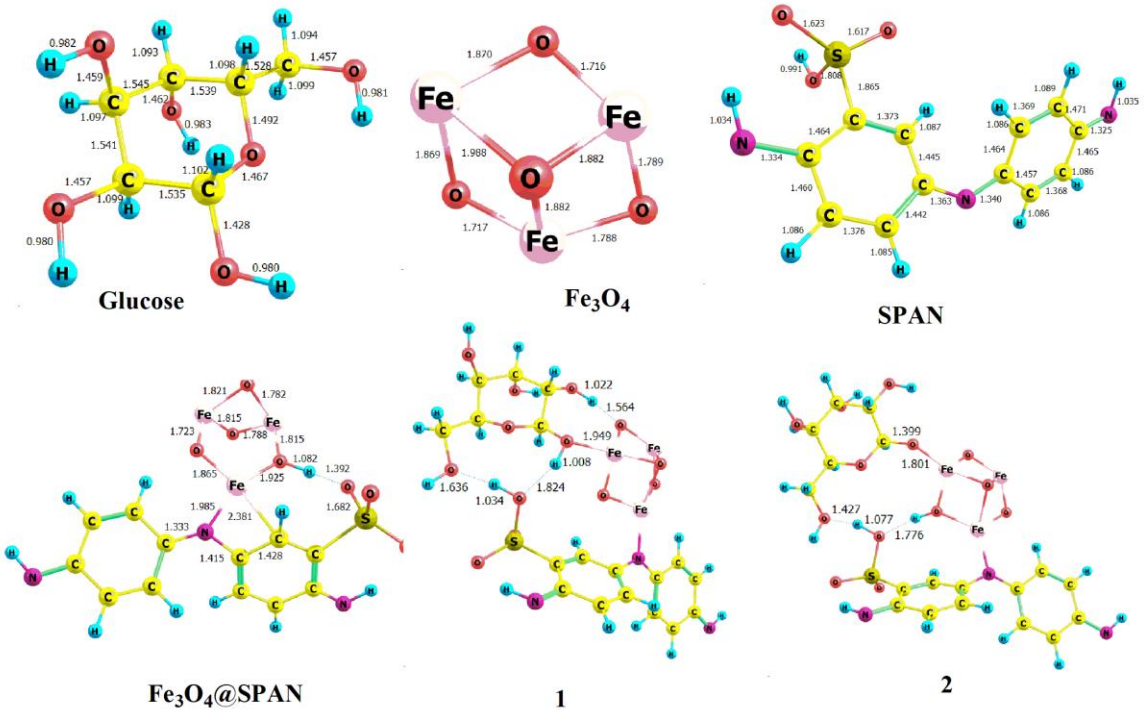

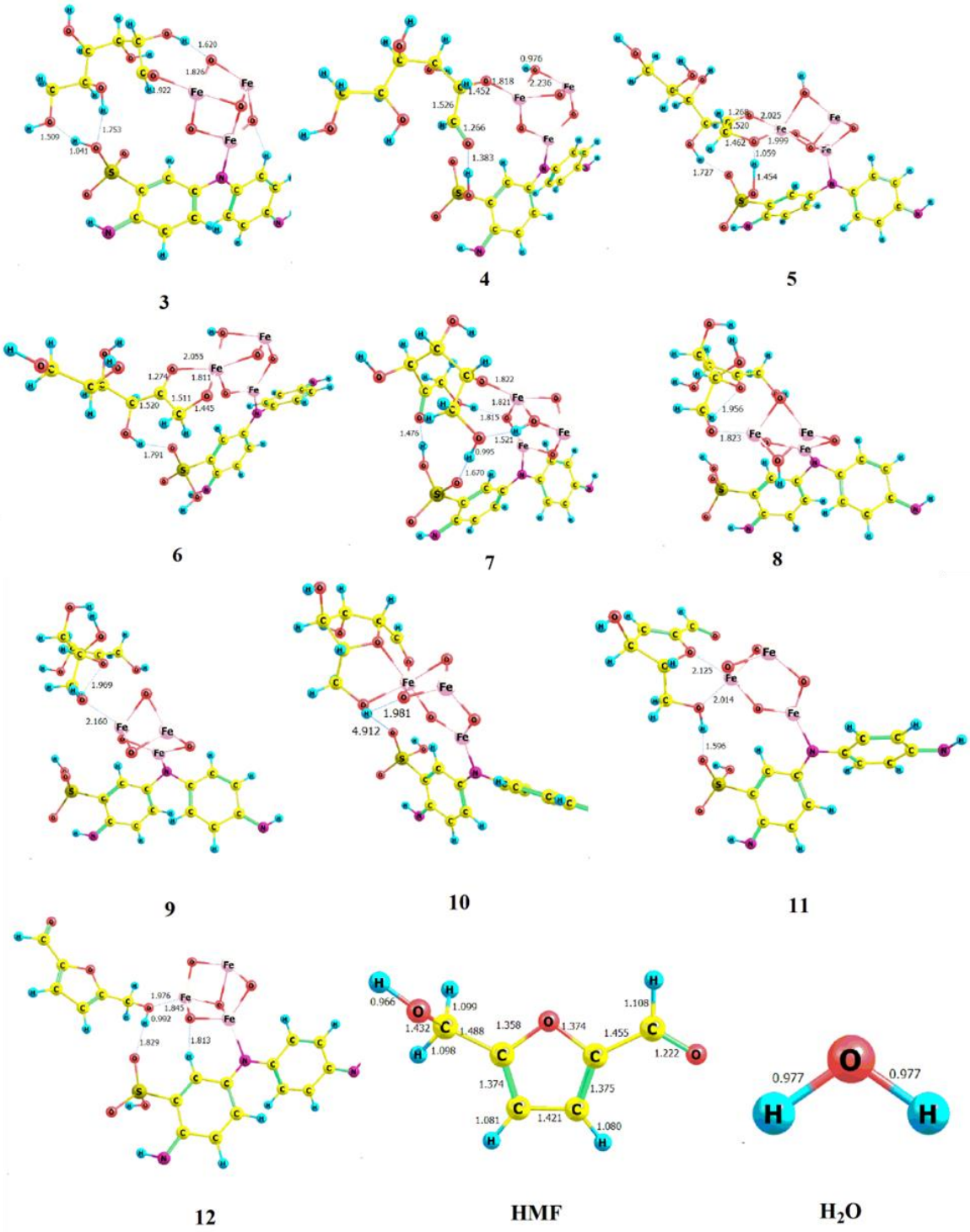

Fig. 5.17. *Optimized structure of all the species (of proposed mechanism) obtained at B3LYP/LANL2DZ level of theory.*

From frequency calculations, we have found that all the species had real and positive frequency values, implying that all the species are stable. Furthermore, zero-point energy were also obtained along with thermochemical data. The absolute value of total energy, Enthalpy and Gibbs free energy of all species are given in Table 5.11. Table 5.12

shows the standard reaction enthalpy ($\Delta_r H^\circ$) and Gibbs free energy ($\Delta_r G^\circ$) calculated from these values for the different reaction steps.

Table 5.11. *Absolute value of total energy, enthalpy and Gibbs free energy of all the species calculated at the B3LYP/LANL2DZ level of theory. (Values are given in Hartree)*

Species	Total energy (E_0)	Enthalpy (H)	Gibbs free energy (G)
SPAN	-862.695864	-862.67763	-862.742907
Glucose	-686.902943	-686.889578	-686.940691
Fe_3O_4	-671.080018	-671.071624	-671.112883
Fe_3O_4@SPAN	-1533.92593	-1533.899156	-1533.983907
1	-2220.930967	-2220.89101	-2221.004541
2	-2220.957194	-2220.916919	-2221.032468
3	-2220.879873	-2220.839668	-2220.954086
4	-2220.980305	-2220.937534	-2221.060136
5	-2221.024305	-2220.982882	-2221.099255
6	-2220.99015	-2220.947553	-2221.069047
7	-2220.908471	-2220.868006	-2220.981648
8	-2221.00245	-2220.960562	-2221.078644
9	-2220.934408	-2220.893799	-2221.006825
10	-2144.499703	-2144.459175	-2144.576744
11	-2068.138474	-2068.099291	-2068.213622
12	-1991.734584	-1991.697354	-1991.810045
HMF	-457.795986	-457.786611	-457.829944
H_2O	-76.393554	-76.389773	-76.411216

Table 5.12. *Standard reaction enthalpy ($\Delta_r H^0$) and Gibbs free energy ($\Delta_r G^0$) for the reaction steps at B3LYP/LANL2DZ level of theory. (Values are given in kcal/mol)*

Reaction Steps	$\Delta_r H^0$	$\Delta_r G^0$
1 →2	-16.26	-17.52
2 →3	48.48	49.19
3→4	-61.41	-66.55
4 →5	-28.46	-24.55
5 →6	22.17	18.96

6 →7	49.92	54.84
7→8	-58.08	-60.87
8→9	41.89	45.07
9 →10 + H_2O	53.24	-61.99
10 →11+H_2O	-18.76	-30.18
11→12 + H_2O	-17.46	69.04

Table 5.12 shows that the reaction steps 1→2, 3→4, 4→5, 7→8, 9→10 + H_2O and 10→11+H_2O (except 9→10 + H_2O step) have $\Delta_rG^0 < 0$ and $\Delta_rH^0 < 0$. This suggest that these steps are exothermic and are spontaneous in nature.

All the species involved in the mechanism are explored in the potential energy diagram. For this we have used absolute energy of all the species given in Table 5.11. We have also determined relative energy of all the species with respect to SPAN, Fe_3O_4 and glucose and are reported in Table 5.13. With the help of Table 5.13, we have explored all the species on the potential energy diagram as shown in Fig. 5.18.

Table 5.13. *Relative energy of all the species with respect to SPAN, Fe_3O_4 and Glucose calculated at the B3LYP/LANL2DZ level of theory.*

Species	**ΔE**
SPAN+Fe3O4+Glucose	0.00
Fe3O4@SPAN+Glucose	-94.16
1	-158.22
2	-174.68
3	-126.16
4	-189.18
5	-216.79
6	-195.36
7	-144.11
8	-203.08
9	-160.38
10+H_2O	-134.56
11 + 2H_2O	-154.84
12 +3H_2O	-148.36

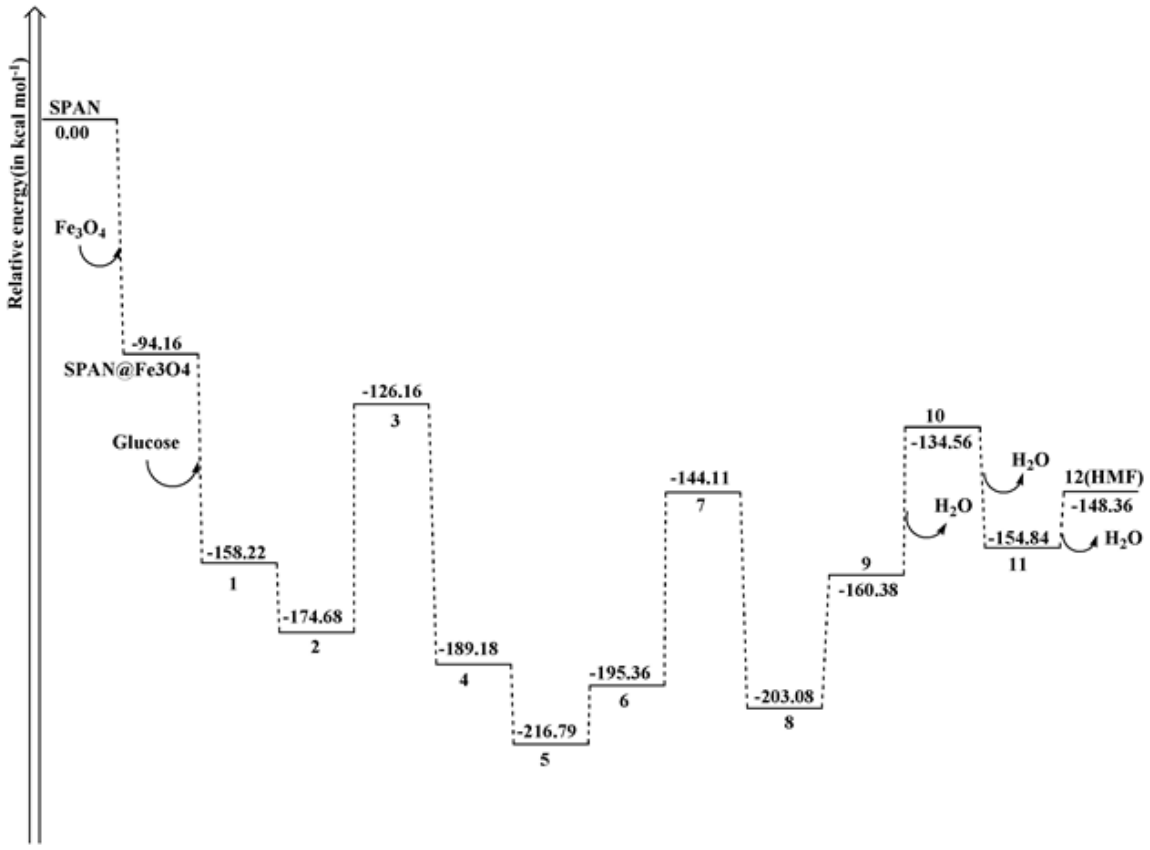

Fig. 5.18*. Potential energy diagram for the dehydration of glucose to HMF using Fe_3O_4@SPAN obtained at B3LYP/LANL2DZ level of theory.*

From Fig. 5.18, it is clear that energy decreases in three successive steps (SPAN→SPAN@Fe_3O_4, SPAN@Fe_3O_4→ 1, and 1→2). The energy value of structure 1 relative to SPAN@Fe_3O_4 was found to be -64.16 kcal mol^{-1} while energy of structure 2 relative to structure 1 was -16.46 kcal mol^{-1}. On the other hand, in step 2→3, the energy value was increased by 48.52 kcal mol^{-1} relative to structure 2. In the next two steps, 3→4 and 4→5, the energy values were found to be -63.02 kcal mol^{-1} and -27.61 kcal mol^{-1} relative to structures 3 and 4, respectively. Likewise, in steps 5→6 and 6→7, the values of energy were 21.43 kcal mol^{-1} and 51.25 kcal mol^{-1} respectively, relative to structures 5 and 6. For the step 7→8, the value of energy was found to be -58.97 kcal mol^{-1}. In the next two successive steps i.e., 8→9 and 9→10, energy increases relative to structures 8 and 9. In step 9→10, one water molecule has been removed. In step 10→11, energy further decreases by -20.28 kcal mol^{-1} with removal of one more water molecule. In the last step, structure 11 finally converts into HMF with further removal of H_2O. In this step energy of HMF + H_2O was slightly increased relative to structure 11. Thus, it can be concluded that

the results of the computational study corroborate well with the proposed mechanism of dehydration of glucose to HMF using Fe_3O_4@SPAN catalyst.

5.6. Conclusion

In conclusion, we have developed a bifunctional catalyst, Fe_3O_4 embedded sulfonated polyaniline, Fe_3O_4@SPAN with well-balanced Lewis-Brønsted acid sites for the transformation of *Saccharum spontaneum* derived glucose and banana peduncle derived glucose to HMF. The catalyst showed excellent activity with glucose conversion of ~100% and HMF yield of ~75%, after being optimized through CCD-based RSM and MLP-based ANN models. The optimum reaction conditions were found to be 40 mg catalyst loading, 150°C, 4 h, and the use of (DMSO/Water) solvent system in the ratio of 4:1. We established that Fe_3O_4 functions as a Lewis acid, inducing glucose to isomerize into fructose *via* ring opening, whereas the H-bonded -SO_3H groups are responsible for fructose dehydration to HMF. The magnetic Fe_3O_4 nanoparticle incorporated in the polyaniline matrix enables easy recovery of the catalyst by magnetic separation. Based on the results, a possible reaction mechanism over the catalyst was also proposed. The proposed mechanism was further established by DFT study where we have explored the catalytic dehydration of glucose to HMF using x-Fe_3O_4@SPAN-y/z-based catalyst *via* the potential energy diagram and thermo-chemical parameters. Furthermore, the chemical bonding of -SO_3H groups on the backbone of the polyaniline chain permits the polymer catalyst to be recyclable for at least five runs without significant activity loss. As a result, the current study provides a novel approach for converting biomass-derived glucose to HMF using a bifunctional Fe_3O_4@SPAN catalyst with easy preparation, high activity, and high stability.

References

[1] Fan, W., Verrier, C., Queneau, Y., and Popowycz, F. 5-Hydroxymethylfurfural (HMF) in organic synthesis: a review of its recent applications towards fine chemicals. *Current Organic Synthesis*, 16(4):583-614, 2019.

[2] Nishimura, S., Ikeda, N., and Ebitani, K. Selective hydrogenation of biomass-derived 5-hydroxymethylfurfural (HMF) to 2, 5-dimethylfuran (DMF) under atmospheric hydrogen pressure over carbon supported PdAu bimetallic catalyst. *Catalysis Today*, 232:89-98, 2014.

[3] Sajid, M., Zhao, X., and Liu, D. Production of 2, 5-furandicarboxylic acid (FDCA) from 5-hydroxymethylfurfural (HMF): recent progress focusing on the chemical-catalytic routes. *Green Chemistry*, 20(24):5427-5453, 2018.

[4] Shen, Y., Sun, J. K., Yi, Y. X., Wang, B., Xu, F., and Sun, R. C. One-pot synthesis of levulinic acid from cellulose in ionic liquids. *Bioresource Technology*, 192:812-816, 2015.

[5] Xia, Q. N., Cuan, Q., Liu, X. H., Gong, X. Q., Lu, G. Z., and Wang, Y. Q. Pd/$NbOPO_4$ multifunctional catalyst for the direct production of liquid alkanes from aldol adducts of furans. *Angewandte Chemie*, 126(37):9913-9918, 2014.

[6] Li, Y., Liu, H., Song, C., Gu, X., Li, H., Zhu, W., Yin, S., and Han, C. The dehydration of fructose to 5-hydroxymethylfurfural efficiently catalyzed by acidic ion-exchange resin in ionic liquid. *Bioresource Technology*, 133:347-353, 2013.

[7] Atanda, L., Silahua, A., Mukundan, S., Shrotri, A., Torres-Torres, G., and Beltramini, J. Catalytic behaviour of TiO_2–ZrO_2 binary oxide synthesized by sol–gel process for glucose conversion to 5-hydroxymethylfurfural. *RSC Advances*, 5(98):80346-80352, 2015.

[8] Perez, G. P., and Dumont, M. J. Production of HMF in high yield using a low cost and recyclable carbonaceous catalyst. *Chemical Engineering Journal*, 382:122766, 2020.

[9] Pagan-Torres, Y. J., Wang, T., Gallo, J. M. R., Shanks, B. H., and Dumesic, J. A. Production of 5-hydroxymethylfurfural from glucose using a combination of Lewis and Brønsted acid catalysts in water in a biphasic reactor with an alkylphenol solvent. *Acs Catalysis*, 2(6):930-934, 2012.

[10] Eminov, S., Filippousi, P., Brandt, A., Wilton-Ely, J. D., and Hallett, J. P. Direct catalytic conversion of cellulose to 5-hydroxymethylfurfural using ionic liquids. *Inorganics*, 4(4):32, 2016.

[11] Zhao, Y., Lu, K., Xu, H., Zhu, L., and Wang, S. A critical review of recent advances in the production of furfural and 5-hydroxymethylfurfural from lignocellulosic biomass through homogeneous catalytic hydrothermal conversion. *Renewable and Sustainable Energy Reviews*, 139:110706, 2021.

[12] Agarwal, B., Kailasam, K., Sangwan, R. S., and Elumalai, S. Traversing the history of solid catalysts for heterogeneous synthesis of 5-hydroxymethylfurfural from carbohydrate sugars: A review. *Renewable and Sustainable Energy Reviews*, 82:2408-2425, 2018.

[13] Fang, X., Wang, Z., Yuan, B., Song, W., Li, S., and Lin, W. Efficient Conversion of Cellulose to 5-Hydroxymethylfurfural in $NaHSO_4/ZrO_2/H_2O$-THF Biphasic System. *ChemistrySelect*, 3(43):12243-12249, 2018.

[14] Silahua-Pavon, A. A., Espinosa-Gonzalez, C. G., Ortiz-Chi, F., Pacheco-Sosa, J. G., Pérez-Vidal, H., Arévalo-Pérez, J. C., Godavarthi, S., and Torres-Torres, J. G. Production of 5-HMF from glucose using TiO_2-ZrO_2 catalysts: Effect of the sol-gel synthesis additive. *Catalysis Communications*, 129:105723, 2019.

[15] Hara, M., Nakajima, K., and Kamata, K. Recent progress in the development of solid catalysts for biomass conversion into high value-added chemicals. *Science and Technology of Advanced Materials*, 16(3):034903, 2015.

[16] Yang, F., Tong, X., Xia, F., Zheng, C., Qin, L., and Jiang, X. Efficient hydroxymethylfurfural production over phosphoric carbon solid acids. *Catalysis Letters*, 148(7):1848-1855, 2018.

[17] Nahavandi, M., Kasanneni, T., Yuan, Z. S., Xu, C. C., and Rohani, S. Efficient conversion of glucose into 5-hydroxymethylfurfural using a sulfonated carbon-based solid acid catalyst: an experimental and numerical study. *ACS Sustainable Chemistry & Engineering*, 7(14):11970-11984, 2019.

[18] Xu, F., and Zhang, Z. Polyaniline-Grafted VO $(acac)_2$: An Effective Catalyst for the Synthesis of 2, 5-Diformylfuran from 5-Hydroxymethylfurfural and Fructose. *ChemCatChem*, 7(9):1470-1477, 2015.

[19] Zhu, L., Dai, J., Liu, M., Tang, D., Liu, S., and Hu, C. Formyl-Modified Polyaniline for the Catalytic Dehydration of Fructose to 5-Hydroxymethylfurfural. *ChemSusChem*, 9(16):2174-2181, 2016.

[20] Dai, J., Zhu, L., Tang, D., Fu, X., Tang, J., Guo, X., and Hu, C. Sulfonated polyaniline as a solid organocatalyst for dehydration of fructose into 5-hydroxymethylfurfural. *Green Chemistry*, 19(8):1932-1939, 2017.

[21] Rai, S. K., and Mukherjee, A. K. Statistical optimization of production, purification and industrial application of a laundry detergent and organic solvent-stable subtilisin-like serine protease (Alzwiprase) from *Bacillus subtilis* DM-04. *Biochemical Engineering Journal*, 48:173-180, 2010.

[22] Roy, J. K., Rai, S. K., and Mukherjee, A. K. Characterization and application of a detergent-stable alkaline α-amylase from *Bacillus subtilis* strain AS-S01a. *International Journal of Biological Macromolecules*, 50:219-229, 2012.

[23] Baruah, J., Chaliha, C., Kalita, E., Nath, B. K., Field, R. A., and Deb, P. Modelling and optimization of factors influencing adsorptive performance of agrowaste-derived Nanocellulose Iron Oxide Nanobiocomposites during remediation of Arsenic contaminated groundwater. *International Journal of Biological Macromolecules*, 164:53-65, 2020.

[24] Onu, C. E., Nwabanne, J. T., Ohale, P. E., and Asadu, C. O. Comparative analysis of RSM, ANN and ANFIS and the mechanistic modeling in eriochrome black-T dye adsorption using modified clay. *South African Journal of Chemical Engineering*, 36:24-42, 2021.

[25] Choudhuri, I., Bhauriyal, P., and Pathak, B. Recent advances in graphene-like 2D materials for spintronics applications. *Chemistry of Materials*, 31(20):8260-8285, 2019.

[26] Stephens, P. J., Devlin, F. J., Chabalowski, C. F., and Frisch, M. J. Ab initio calculation of vibrational absorption and circular dichroism spectra using density functional force fields. *The Journal of Physical Chemistry*, 98(45):11623-11627, 1994.

[27] Meng, G., Lam, N. Y., Lucas, E. L., Saint-Denis, T. G., Verma, P., Chekshin, N., and Yu, J. Q. Achieving site-selectivity for C–H activation processes based on distance and geometry: a carpenter's approach. *Journal of the American Chemical Society*, 142(24):10571-10591, 2020.

[28] Antonetti, C., Melloni, M., Licursi, D., Fulignati, S., Ribechini, E., Rivas, S., Parajo, J. C., Cavani, F., and Galletti, A. M. R. Microwave-assisted dehydration of fructose and inulin to HMF catalyzed by niobium and zirconium phosphate catalysts. *Applied Catalysis B: Environmental*, 206:364-377, 2017.

[29] Dias, A. S., Lima, S., Carriazo, D., Rives, V., Pillinger, M., and Valente, A. A. Exfoliated titanate, niobate and titanoniobate nanosheets as solid acid catalysts for the liquid-phase dehydration of D-xylose into furfural. *Journal of Catalysis*, 244(2):230-237, 2006.

[30] Qiu, G., Huang, C., Sun, X., and Chen, B. Highly active niobium-loaded montmorillonite catalysts for the production of 5-hydroxymethylfurfural from glucose. *Green Chemistry*, 21(14):3930-3939, 2019.

[31] Wang, Y., Wang, Y., Tang, J., Xia, Y., and Zheng, G. Aqueous Li-ion cells with superior cycling performance using multi-channeled polyaniline/Fe_2O_3 nanotube anodes. *Journal of Materials Chemistry A*, 2(47):20177-20181, 2014.

[32] Liao, Y., Strong, V., Chian, W., Wang, X., Li, X. G., and Kaner, R. B. Sulfonated polyaniline nanostructures synthesized via rapid initiated copolymerization with controllable morphology, size, and electrical properties. *Macromolecules*, 45(3):1570-1579, 2012.

[33] Li, G. C., Zhang, C. Q., Peng, H. R., Chen, K. Z., and Zhang, Z. K. Hollow self-doped polyaniline micro/nanostructures: Microspheres, aligned pearls, and nanotubes. *Macromolecular Rapid Communications*, 29(24):1954-1958, 2008.

[34] Park, B. D., Wi, S. G., Lee, K. H., Singh, A. P., Yoon, T. H., and Kim, Y. S. X-ray photoelectron spectroscopy of rice husk surface modified with maleated polypropylene and silane. *Biomass and Bioenergy*, 27(4):353-363, 2004.

[35] Iida, H., Takayanagi, K., Nakanishi, T., and Osaka, T. Synthesis of Fe_3O_4 nanoparticles with various sizes and magnetic properties by controlled hydrolysis. *Journal of Colloid and Interface Science*, 314(1):274-280, 2007.

[36] Wang, L., Jia, X., Li, Y., Yang, F., Zhang, L., Liu, L., Ren, X., and Yang, H. Synthesis and microwave absorption property of flexible magnetic film based on graphene oxide/carbon nanotubes and Fe_3O_4 nanoparticles. *Journal of Materials Chemistry A*, 2(36):14940-14946, 2014.

[37] Mahto, T. K., Chandra, S., Haldar, C., and Sahu, S. K. Kinetic and thermodynamic study of polyaniline functionalized magnetic mesoporous silica for magnetic field guided dye adsorption. *RSC Advances*, 5(59):47909-47919, 2015.

[38] Zhao, S. Y., Lee, D. G., Kim, C. W., Cha, H. G., Kim, Y. H., and Kang, Y. S. Synthesis of magnetic nanoparticles of Fe_3O_4 and $CoFe_2O_4$ and their surface modification by surfactant adsorption. *Bulletin of the Korean Chemical Society*, 27(2):237-242, 2006.

[39] Rodulfo-Baechler, S. M., González-Cortés, S. L., Orozco, J., Sagredo, V., Fontal, B., Mora, A. J., and Delgado, G. Characterization of modified iron catalysts by X-ray diffraction, infrared spectroscopy, magnetic susceptibility and thermogravimetric analysis. *Materials Letters*, 58(20):2447-2450, 2004.

[40] Díaz, E., Ordóñez, S., Vega, A., and Coca, J. Evaluation of different zeolites in their parent and protonated forms for the catalytic combustion of hexane and benzene. *Microporous and Mesoporous Materials*, 83(1-3):292-300, 2005.

[41] Mallesham, B., Sudarsanam, P., and Reddy, B. M. Eco-friendly synthesis of bio-additive fuels from renewable glycerol using nanocrystalline SnO_2-based solid acids. *Catalysis Science & Technology*, 4(3):803-813, 2014.

[42] Mohammadi, A., and Barikani, M. Synthesis and characterization of superparamagnetic Fe_3O_4 nanoparticles coated with thiodiglycol. *Materials Characterization*, 90:88-93, 2014.

[43] Wang, X., Liu, Y., Han, H., Zhao, Y., Ma, W., and Sun, H. Polyaniline coated Fe_3O_4 hollow nanospheres as anode materials for lithium-ion batteries. *Sustainable Energy & Fuels*, 1(4):915-922, 2017.

[44] Gao, Q., Zhao, A., Gan, Z., Tao, W., Li, D., Zhang, M., Guo, H., Wang, D., Sun, H., Mao, R., and Liu, E. Facile fabrication and growth mechanism of 3D flower-like Fe_3O_4 nanostructures and their application as SERS substrates. *CrystEngComm*, 14(14):4834-4842, 2012.

[45] Zhu, X. D., Wang, K. X., Yan, D. J., Le, S. R., Ma, R. J., Sun, K. N., and Liu, Y. T. Creating a synergistic interplay between tubular MoS_2 and particulate Fe_3O_4 for improved lithium storage. *Chemical Communications*, 51(59):11888-11891, 2015.

[46] Mu, B., Tang, J., Zhang, L., and Wang, A. Preparation, characterization and application on dye adsorption of a well-defined two-dimensional superparamagnetic clay/polyaniline/Fe_3O_4 nanocomposite. *Applied Clay Science*, 132:7-16, 2016.

[47] Li, L., Li, Y., Gao, S., and Koshizaki, N. Ordered Co_3O_4 hierarchical nanorod arrays: tunable superhydrophilicity without UV irradiation and transition to superhydrophobicity. *Journal of Materials Chemistry*, 19(44):8366-8371, 2009.

[48] Zheng, L., Xiong, L., Liu, C., and Jin, L. Electrochemical synthesis of a novel sulfonated polyaniline and its electrochemical properties. *European Polymer Journal*, 42(10):2328-2333, 2006.

[49] Du, J., Liu, Z., Han, B., Li, Z., Zhang, J., and Huang, Y. One-pot synthesis of the macroporous polyaniline microspheres and Ag/polyaniline core-shell particles. *Microporous and Mesoporous Materials*, 84(1-3):254-260, 2005.

[50] Lowell, S., Shields, J. E., Thomas, M. A., and Thommes, M. *Characterization of porous solids and powders: surface area, pore size and density*. Springer Science & Business Media, 2006.

[51] Liu, W., Ji, J., Chen, H., and Ye, C. Optimal color design of psychological counselling room by design of experiments and response surface methodology. *PloS one*, 9(3):e90646, 2014.

[52] Chidambaram, R. Isotherm modelling, kinetic study and optimization of batch parameters using response surface methodology for effective removal of Cr (VI) using fungal biomass. *PloS one*, 10(3):e0116884, 2015.

[53] Shang, H., Zhou, H., Duan, M., Li, R., Wu, H., and Lou, Y. Extraction condition optimization and effects of drying methods on physicochemical properties and antioxidant activities of polysaccharides from comfrey (*Symphytum officinale* L.) root. *International Journal of Biological Macromolecules*, 112:889-899, 2018.

[54] Ayawei, N., Ebelegi, A. N., and Wankasi, D. Modelling and interpretation of adsorption isotherms. *Journal of Chemistry*, 2017:1-11, 2017.

[55] Wakkel, M., Khiari, B., and Zagrouba, F. Textile wastewater treatment by agro-industrial waste: equilibrium modelling, thermodynamics and mass transfer mechanisms of cationic dyes adsorption onto low-cost lignocellulosic adsorbent. *Journal of Taiwan Institute of Chemical Engineers*, 96:439-452, 2019.

[56] Geyikçi, F., Kılıç, E., Çoruh, S., and Elevli, S. Modelling of lead adsorption from industrial sludge leachate on red mud by using RSM and ANN. *Chemical Engineering Journal*, 183:53-59, 2012.

[57] Elsayed, I., Mashaly, M., Eltaweel, F., and Jackson, M. A. Dehydration of glucose to 5-hydroxymethylfurfural by a core-shell Fe_3O_4@SiO_2-SO_3H magnetic nanoparticle catalyst. *Fuel*, 221:407-416, 2018.

[58] Jiang, N., Qi, W., Wu, Z., Su, R., and He, Z. "One-pot" conversions of carbohydrates to 5-hydroxymethylfurfural using Sn-ceramic powder and hydrochloric acid. *Catalysis Today*, 302:94-99, 2018.

[59] Wang, Qing, Mingxing Fu, Xiaojun Li, Runfeng Huang, Rainer E. Glaser, and Lili Zhao. Aluminum alkoxy-catalyzed biomass conversion of glucose to 5-hydroxymethylfurfural: Mechanistic study of the cooperative bifunctional catalysis. *Journal of Computational Chemistry* 40(16):1599-1608, 2019.

[60] Zhou, C., Zhao, J., Yagoub, A. E. A., Ma, H., Yu, X., Hu, J., Bao, X., and Liu, S. Conversion of glucose into 5-hydroxymethylfurfural in different solvents and catalysts: Reaction kinetics and mechanism. *Egyptian Journal of Petroleum*, 26(2):477-487, 2017.

[61] Patrylak, L., Konovalov, S., Pertko, O., Yakovenko, A., Povazhnyi, V., and Melnychuk, O. Obtaining Glucose-Based 5-Hydroxymethylfurfural on Large-Pore Zeolites. *Eastern-European Journal of Enterprise Technologies*, 2(6):110, 2021.

[62] Hoang, P. H., Dat, N. M., Cuong, T. D., and Tung, D. T. Production of 5-hydroxymethylfurfural (HMF) from rice-straw biomass using a HSO_3–ZSM-5 zeolite catalyst under assistance of sonication. *RSC Advances*, 10(23):13489-13495, 2020.

[63] Zhao, J., Zhou, C., He, C., Dai, Y., Jia, X., and Yang, Y. Efficient dehydration of fructose to 5-hydroxymethylfurfural over sulfonated carbon sphere solid acid catalysts. *Catalysis Today*, 264:123-130, 2016.

[64] Tomer, R., and Biswas, P. Dehydration of glucose/fructose to 5-hydroxymethylfurfural (5-HMF) over an easily recyclable sulfated titania (SO_4^{2-}/TiO_2) catalyst. *New Journal of Chemistry*, 44(47):20734-20750, 2020.

[65] Zhang, Y., Shen, Y., Chen, Y., Yan, Y., Pan, J., Xiong, Q., Shi, W., and Yu, L. Hierarchically carbonaceous catalyst with Brønsted–Lewis acid sites prepared through Pickering HIPEs templating for biomass energy conversation. *Chemical Engineering Journal*, 294:222-235, 2016.